

The Impact of Squall-Line-Generated Gravity Waves and Anvil Shading on Simulated Supercell Thunderstorms

by
Michael Montalbano

A thesis submitted to the Graduate Division
in partial fulfillment of the requirements for the degree of
Master of Science in Physics

South Dakota School of Mines and Technology
Rapid City, South Dakota

Date Defended:

Approved by:

Major Professor — Adam J. French, Ph.D., Department of Physics

Date

Graduate Division Representative — Larry D. Pyeatt, Ph.D., Department of Mathematics and Computer Science

Date

Committee Member — Vladimir L. Sobolev, Ph.D., Department of Physics

Date

Committee Member — William J. Capehart, Ph.D., Department of Civil and Environmental Engineering

Date

Head of the Department of Physics — Richard W. Schnee, Ph.D.

Date

Dean of Graduate Education — Maribeth H. Price, Ph.D.

Date

Copyright © 2019, Michael Montalbano
All Rights Reserved

Abstract

Convective storms modify their environments in multiple ways, including through cloud-radiative effects and gravity-buoyancy waves. In this study, we investigate how these modifications affect storm development. In particular, we examine how a supercell is affected by both the gravity waves generated by a squall line and the anvil formed by a supercell. We focus on whether these influences impact supercell development and how storms interact with each other.

To accomplish this task, a series of numerical simulations have been run using the cloud model CM1. Supercell storms were simulated with and without a squall line nearby, and with and without anvil shading effects included in the model. This set of tests makes it possible to isolate how squall line-induced anvil shading and gravity waves affect the structure, intensity, and development of a nearby supercell. Results show that storm interactions are significant. Gravity waves, created by the squall line, weaken the supercell, strongly curtailing its precipitation. Anvil shading also weakens supercells, making them more susceptible to gravity wave-induced perturbations. When both gravity waves and anvil shading are present, the supercell dissipates entirely. In this most realistic case, the storm evolution is significantly different from the idealized case, suggesting that these effects may be an important consideration when forecasting severe convective storms.

Acknowledgments

I would like to thank my advisor, Dr. Adam French, for all of the support he has given me. I thank the Laughing Tea Bowl Sangha for their wisdom, and my family for their guidance. I would also like to thank Matthew Parker at North Carolina State University for the pressure decomposition scripts. Computational resources and data storage were provided by NCAR's Cheyenne Supercomputer. This research was supported by NSF Grant AGS-1339469.

Table of Contents

Abstract	i
Acknowledgments	ii
Table of Contents	iii
List of Figures	v
List of Tables	vi
1 Introduction	1
2 Past Work	3
2.1 Fundamental supercell dynamics	3
2.2 Storm interaction	6
3 Methods	11
3.1 Model set-up	11
3.2 Dynamic Analysis	13
4 Results	17
4.1 Overview of combined-shaded simulation	17
4.1.1 Overall storm evolution	17
4.1.2 Gravity wave	17
4.1.3 Anvil shading	18
4.2 Overview and comparisons between supercells	19
4.3 Relation between observed behavior and hypothesized mechanisms	22
4.4 Evaluation of hypothesized mechanisms	24
4.4.1 Role of gravity wave and anvil-shading induced environmental changes	24
4.4.2 Role of direct influence of gravity wave on supercell's midlevel updraft	25
4.4.3 Role of anvil-shading on "missing" recovery phase in CS	30
5 Discussion	50
6 Conclusion	52
6.1 Summary	52
6.2 Broader Implications	53
6.3 Future Work	53
Bibliography	55

Vita	58
-------------	----

List of Figures

3.1	Model configuration	15
3.2	Initial sounding	16
4.1	Simulated radar reflectivity	32
4.2	Hovmoller of CS	33
4.3	Gravity wave	34
4.4	Anvil shading	35
4.5	Overview	36
4.6	Time-series of storm metrics	37
4.7	Time-series of environment metrics	38
4.8	7 km AGL updraft profile	39
4.9	Vertical total accelerations profile	40
4.10	Vertical buoyant accelerations profile	41
4.11	Vertical dynamic accelerations profile	42
4.12	1 km AGL updraft profile	43
4.13	Horizontal total accelerations profile	44
4.14	Horizontal dynamic accelerations profile	45
4.15	Vertical dynamic pressure profile	46
4.16	Horizontal buoyant accelerations profile	47
4.17	Vertical buoyancy profile	48
4.18	Surface temperature gradient	49

List of Tables

3.1 Model Configuration	12
-----------------------------------	----

Chapter 1

Introduction

Supercells are dangerous storms that cause fatalities and economic damage every year. They spawn deadly tornadoes, capable of devastating towns with their fierce winds. They also generate vast swaths of precipitation, showering hundreds of square kilometers with rain and hail. Over the past seventy years, we have learned a great deal about these storms. Improving our understanding has changed how our society reacts to severe weather. As predictive models have improved, so has our ability to warn endangered populations and mitigate risk. This research is part of an effort to study these storms under increasing complexity, and thus reduce our current uncertainty.

Supercells are often studied using numerical simulations. In controlled settings, supercells are most commonly initiated using an idealized sounding in horizontally homogeneous environments, in which the base-state kinematic and thermodynamic profile does not vary across the domain. While this is far simpler than real-world environments, with all their variations, this type of experiment provides for controlled hypothesis testing and isolates the role of individual parameters. While such studies have yielded vast physical insight into supercell mechanics, they are simplified versions of a real-world supercell. In one way, simplification arises because supercells are often simulated discretely, such that they are the only mode of convection in a simulation. But in nature, they often form alongside other storms. Another way supercells are simplified is through neglecting cloud-radiative effects. To date, these have been generally treated as higher order effects, and so are “justifiably” left out in the interest of studying basic principles.

Our study seeks to bridge this gap by studying the exact impact of these higher order terms. First, instead of using an idealized sounding, we use a real-world sounding taken from a day of high convection. On this day, both a squall line and supercell were found in close proximity

to one another. We then proceed to simulate not just a supercell, but both a squall line and a supercell. To bring it even closer to reality, we simulate anvil shading as well. Altogether, this set-up allows us to study a supercell in an environment that is more realistic than many past studies. Ultimately, the results of this work may inform future forecast model development, leading to more accurate severe thunderstorm forecasts.

We simulate four supercells. Each begins in an identical environment, but one that changes based on differing model configurations. These four simulations range from a discrete supercell simulated without anvil shading effects (the idealized case) to a supercell simulated with anvil shading and a nearby squall line (the most realistic case). The intermediate cases include an isolated supercell with anvil shading, and a supercell with a nearby squall line but without anvil shading. By comparing each of these simulations against each other, we hope to identify the importance of higher-order effects like storm-interactions and anvil-shading on supercell thunderstorms.

The past work is described in chapter 2. The design of the experiment and methods are explained in chapter 3. The results are presented in chapter 4, and discussed in chapter 5. Our conclusion appears in chapter 6.

Chapter 2

Past Work

2.1 Fundamental supercell dynamics

Storm science has long been motivated by a desire to better predict deadly events. In the very early days, it was not yet clear which type of storm was responsible for the wild tornadoes of the Midwest. Once Fujita (1958) had correlated damage tracks with radar reports, researchers were able to pinpoint the tornadic storms: supercells. Browning (1964) saw that these storms possessed a single, rotating updraft. Later, Lemon and Doswell III (1979) found that these storms had a unique radar signature and structure. Precipitation falls in two flanks that form a bird-like shape. The structure of the storm depends upon the mesocyclone, which is a single, rotating updraft that reaches from the surface up at least 10 km. It rotates near a curved area in the radar image, known as the hook-echo. Early research characterized these storms, establishing their common features and behaviors. Critically, forecasters applied this knowledge to spot dangerous storms and issue life-saving forecasts.

In the 1970's and 1980's, meteorologists developed early computational models (Wilhelmson and Wicker 2001). By solving the equations of motion and parameterizing for micro-physics and turbulence, scientists created models capable of simulating convection (Klemp and Wilhelmson 1978). With them, researchers experimented and eventually succeeded in creating realistic thunderstorms, yielding new information that was unobtainable *in situ* (Weisman and Klemp 1982). This led to a boon in understanding about the wind fields and temperature gradients within storms. Scientists began answering questions that had hounded the science for years (Klemp and Wilhelmson 1978).

One of the questions that dogged researchers concerned supercell motion. Browning (1964) had observed that supercells moved to the right of the mean wind, so that a supercell in a northeast wind would travel more quickly to the east than the north. It had also been shown

that supercells preferred environments with directional wind shear, in which winds westward surface winds veered clockwise to eastward upper-level winds (Maddox 1976). By solving for pressure, researchers showed that the interaction between a storm's mesocyclone and veering winds led to a pressure perturbations that favored upward motion on the updraft's right side (Weisman and Klemp 1984). Therefore, regeneration of the updraft would always prefer the right side and lead to a rightward moving storm. This interaction between a storm and its environment was, and remains, a common lens used to study storms.

A major goal of the field had been to predict the likelihood of severe weather using measurements of a given environment. Weisman and Klemp (1982) sought to determine whether "the great complexity of convective storm evolution may be largely governed by a limited number of observable features of the environment". There had been observations that showed certain environments perhaps being more conducive to tornadic thunderstorms, but the link was not theoretically understood. Early research sought to illuminate the connection between the environment and storm type. They used parameter studies to test how the environment affected storm type. One parameter they used was buoyancy, which is defined as:

$$B = g \left[\frac{\theta'}{\theta} + 0.6(q_v - \bar{q}_v) \right] \quad (2.1)$$

where θ is the potential temperature and q_v is water vapor mixing ratio. Parcels of air that are hotter than the overlying environment and/or more moist possess more buoyancy. These parcels are convectively unstable, so they lift easily into an updraft. The other parameter they used was bulk vertical wind shear over the 0 to 6 km Above Ground Level (AGL) layer, which is defined as:

$$\vec{V}_{Shr} = \vec{V}_{6km} - \vec{V}_{sfc}. \quad (2.2)$$

Additionally, the wind profile needed to change direction and magnitude as it rose in height. They discovered how environmental parameters control storm type and encapsulated it in the Richardson number, which defines the balance of buoyancy and vertical wind shear in an envi-

ronment:

$$R = \frac{B}{\frac{1}{2}\vec{V}_{Shr}^2} \quad (2.3)$$

Supercells form most readily when $10 \leq R \leq 50$. Buoyancy is captured in the environmental parameter Convective Available Convective Energy (CAPE),

$$CAPE = \int_{EL}^{LFC} Bdz \quad (2.4)$$

where EL is the equilibrium level, usually above 15 km AGL, and LFC is the level of free convection, usually above 1 km AGL. Ultimately, Weisman and Klemp (1982) concluded that at least $1500 J kg^{-1}$ of CAPE and $20 m/s$ of \vec{V}_{Shr} was needed for splitting supercell storms. Supercell thunderstorms were found to be more likely in environments with high buoyancy and vertical wind shear.

This dependence on high CAPE and vertical wind shear has also been confirmed by observational studies, which examine real-world supercells and their environments. Thompson et al. (2003) found that there was a tendency in supercells for greater CAPE and vertical wind shear. As these values decreased, storms tended to be either non-tornadic supercells or nonsupercell storms. These storm types have also been distinguished by differing low-level environments. Higher values of vertical wind shear in the lowest 1 km are found in tornadic supercells more often than in non-tornadic supercell or nonsupercell storms (Markowski et al. 2003). Ultimately, the strongest supercells are associated with the highest values of CAPE, 0-6 km AGL vertical wind shear, and 0-1 km AGL vertical wind shear.

Another major leap in understanding came in understanding how supercells regenerate mesocyclones throughout their lifetime, which is done through the process of cyclic-mesocyclogenesis. The mesocyclone is the defining characteristic of supercells, and is critical to storm evolution. By simulating supercells using an idealized sounding, Adelman et al. (1999) saw that a single supercell could periodically produce mesocyclones. It was found that mesocyclones undergo cycles whereby one decays and is forced rearward into the storm. As it decays, a new mesocyclone forms on the storm's gust front, which is the eastern edge separating the storm's cold

pool from the environment's inflow. Thus, mesocyclones routinely decay and regenerate inside supercell thunderstorms (Adlerman et al. 1999). Adlerman and Droege (2005) explored the "role played by the ambient environment in delineating cyclic from noncyclic mesocyclones as well as the extent to which the environment influences the timing and character of mesocyclone occlusions." Specifically, they found that higher shear enhanced mesocyclogenesis at the surface, again showing that the environment was fundamental to governing how supercells evolved. Not only is shear important to storm organization, it also controls internal development.

The key findings of much of the early research was that CAPE and shear were found to be fundamental to storm structure. While individual supercells vary based on many other parameters, researchers can use CAPE and shear to judge how favorable an environment is for supercells. While they are often thought of as static indicators of the large-scale environment, any changes in these quantities may lead to changes in storm behavior [e.g. Richardson et al. (2007), Ziegler et al. (2010) papers on environmental heterogeneity]. This early work discovered the leading factors controlling supercell dynamics and paved the way for more complex future work.

2.2 Storm interaction

The leaps in understanding outlined above enabled researchers to expand their vision. Using the knowledge base built during the 1980's, they began to experiment with storms that more closely approximated those found in nature. While early studies focused on storms in very controlled environments, more recent simulations have allowed supercells to develop in evolving environments.

Researchers can create an evolving environment in many different ways. Richardson et al. (2007) varied vertical wind shear horizontally, which allowed their supercells to move from initially favorable environments to eventually unfavorable environments. Similarly, Coffer and Parker (2015) looked at how changes in shear over time affected supercells using a base-state-substitution, which places the supercell in a substituted base-state at each preceding time-step.

Ziegler et al. (2010), on the other hand, led a supercell through an environment with changing low-level stability, with variations in buoyancy and CAPE not vertical wind shear. These so-called parameter studies allow scientists to assess how supercells respond to changing conditions, thereby enriching our understanding of how supercells operate in natural environments.

While supercells may move into a changing environment, they also can modify the environment as they move through, which was shown observationally in Markowski et al. (1998). Early in a supercells's lifetime, they generate a cirrus anvil, which is ice launched vertically through an updraft into the upper troposphere, over 10 km AGL. High-velocity winds blow the ice downstream, forming an optically thick cirrus anvil that shades a storm's upstream environment. The anvil absorbs and scatters downwelling radiation, ultimately attenuating and blocking it from reaching the ground, cooling the surface. Ultimately, Markowski et al. (1998) demonstrated that anvils could cause a temperature gradient of 5 - 7 K between cold shaded and hot unshaded ground, which was worthy of further study.

Frame and Markowski (2010) started by simulating this process, ultimately showing how it affected the surface layer. As a surface shades, vertical motions are suppressed. This lessens the degree to which high velocity winds transport momentum downward to surface winds. Over time, winds in contact with the ground slow down due to friction. These changes to the environment motivated researchers to understand the significance of anvil shading — namely how it affects the low-level shear profile.

Frame and Markowski (2013) studied how these changes affected the development of supercell thunderstorms. In a series of papers, they simulated supercells with anvil shading. Such shaded supercells were weaker than their unshaded counterparts, as they produced less precipitation over shorter lifetimes. In any supercell, there is a balance between the shear of the cold pool and the shear of the inflow. When these two are balanced, the cold pool remains close to the updraft, which enhances lifting and grows the storm. When these two are unbalanced, the cold pool may rush out ahead of the storm, cutting off the updraft from its unstable inflow source. An unfavorable balance occurs when inflow shear is of the same sense as cold pool

shear, which allows the cold pool to rush out. Ultimately, anvil shading was found to affect this process, as it enhanced the shear of the inflow in the same sense as the shear of the cold pool. Thus upsetting the balance, anvil shading caused the cold pool to rush out away from the updraft, displacing it from its source of warm, buoyant air. In such cases when inflow was maximally affected by anvil shading, supercells were found to dissipate entirely.

Not only do supercells alter their environment, but so do nearby storms alter a supercell's environment (French and Parker 2008). Supercells often spawn in diverse environments, containing multiple sources of convection. Each storm perturbs the evolution of every other storm, yet the large-scale analyses of environmental parameters are from deterministic. When multiple thunderstorm organizational modes are present, forecasts become complicated. In particular, supercells are frequently observed in close proximity to squall lines (e.g. French and Parker 2012). Squall-lines are linear complexes of thunderstorms often exceeding 100 km in length. Often, the squall line will merge with the supercell, as the cold pool of the squall line interacts with the supercell's mesocyclone. Observational studies have shown that mergers can either be associated with tornadogenesis (e.g. Wolf et al. 1996) or, instead, enhanced bow echo activity (French and Parker 2012).

More recent studies have examined mergers using computational models, in which supercells and squall lines were allowed to merge in various environments (French and Parker 2014). In some environments mergers were found to act as a possible "instigator" for tornadogenesis, yet in others the merger was simply associated with more damaging winds. In the cases discussed above, the squall lines generally merged with the supercells by overtaking them. By studying the mechanisms governing merger outcomes, these study elucidated the challenges of studying direct storm-to-storm interactions (French and Parker 2014).

One situation that has not seen extensive study is how changes to the environment ahead of an approaching squall line may affect a supercell in this region. Bryan and Parker (2010) presented a unique analysis of how the surface environment changed during a squall passage. Ahead of the storm by 50 km, the environment undergoes changes in CAPE and CIN, and

in both low-level (0.5 - 2 km) and deep-layer (0.5 - 10 km) vertical wind shear. All of these parameters are important to supercell development and modifications to these parameters could affect the development of storms ahead of squall lines.

Squall lines have been found to influence their far upstream environment ($\gtrsim 100$ km) through gravity-buoyancy waves (Fovell 2002). Atmospherically, gravity waves are waves generated to restore equilibrium, which is unbalanced by convection. One wave generating mechanism is the latent heat release in the squall line's updraft. Strong latent release associated with condensation generates a wave of subsidence to dissipate the heat to the local environment (e.g. Nicholls et al. 1991). As this wave of motion moves away from the squall line, it warms and dries the environment via adiabatic compression. This heating can modify important environmental parameters like CAPE, which is sensitive to temperature and moisture. Likewise, gravity wave-induced perturbations to the winds can also affect the vertical shear profile. Both of these parameters are important to supercell dynamics; however the effects of squall line-induced environmental perturbations on nearby supercells has not been studied.

Several studies have observed gravity waves interacting with supercells. These have suggested that gravity waves may increase vorticity and thereby strengthen supercells (Miller and Sanders 1980; Kilduff 1999). More recently, Coleman and Knupp (2008) have focused on the link between vorticity alterations to mesocyclones using observational data. In their case studies, they documented 15 cases of possible gravity wave enhancement of vorticity in supercells. This connection was further verified by a computational model, although the model was only 1-Dimensional. Overall, the researchers found that gravity waves could likely strengthen rotation within mesocyclones, and lead to more powerful supercells. While this study was not definitive, it provides at least one possible way by which gravity waves and supercells may interact.

In light of this past work that establishes the connection between supercells and the environment, squall lines' ability to alter their local environment, and the possible role of gravity waves influencing supercell rotation, the present work seeks a better understanding of how

a nearby squall line can influence a discrete supercell storm. In our case, we simulate this situation using a squall line and supercell in an environment perturbed by anvil shading. By doing so, we study how a supercell will develop under changing conditions, associated with an approaching squall line, similar to what is often observed during severe weather outbreaks. We hypothesize that a supercell will be weakened by squall line- and anvil shading-induced perturbations to the near-storm environment.

Chapter 3

Methods

3.1 Model set-up

We conducted numerical simulations of supercell thunderstorms using Cloud Model 1 (CM1), which is a computational model for deep convection developed by Bryan and Fritsch (2002). CM1 is a numerical model that integrates the 3-Dimensional governing equations for velocity, potential temperature, nondimensional pressure, and mixing ratios for the different forms of water. It is a non-hydrostatic model developed for idealized simulations of convection.

Each simulation used the same base state environment, but they differed in terms of what processes were simulated. Anvil shading was turned on in the SHADED simulations, while an approaching squall line was included in the COMBINED simulations. Anvil shading is absent in CLEAR simulations, and an approaching squall line is absent in SOLO simulations (Figure 3.1). This generated four simulations: SOLO-CLEAR, SOLO-SHADED, COMBINED-CLEAR, and COMBINED-SHADED (Table 1). By comparing between these simulations, we gain insight into how each factor influences supercell evolution.

Radiation was simulated using the National Aeronautics and Space Administration Goddard Cumulus Ensemble radiative transfer model, which is included in the basic CM1 distribution. It simulates both shortwave and longwave radiation, allowing for the absorption, scattering, and emission of radiation by atmospheric constituents, including clouds and gasses (Chou et al. 1998; Chou et al. 1999). The clear simulations are configured by setting the cloud water, rainwater, graupel, and ice mixing ratio equal to zero in the scheme. This results in uniform radiative heating, equal at all grid points, regardless of whether any cloud or precipitation is present. To simulate anvil shading, the radiation scheme was left unaltered such that radiation impacting surface grid points is attenuated by the amount of atmospheric constituents.

Table 3.1: Model Configuration

Model run	Squall line	Anvil Shading
SOLO-CLEAR	No	No
SOLO-SHADED	No	Yes
COMBINED-CLEAR	Yes	No
COMBINED-SHADED	Yes	Yes

The model is initialized using a horizontally homogeneous base state given by a sounding taken from May 24th, 2008 in the Dodge City, Kansas area (Figure 3.2). This sounding was taken ahead of a convective system that contained mature supercells tens of kilometers east of a squall line, both of which were moving to the east. While a sounding created from real data involves more complexity and, perhaps, less generalization than an idealized sounding, it compensates by lending convenience and imparting credibility. Little experimentation is needed to initiate both the squall line and the supercell. The storms thus spawned are similar to what might be found in nature. The squall line was triggered 175 km west of the supercell so that both could develop into mature storms before they interacted.

This sounding has 2763 J kg^{-1} of convective available potential energy (CAPE), 2 J kg^{-1} of convective inhibition (CIN), a $332 \text{ m}^2 \text{ s}^{-2}$ of storm-relative helicity (Figure 3.2) The wind profile is characterized by veering winds which are easterly at the surface and strong westerly in the upper levels. This wind profile results in squall line and supercell motion to the east and east-north-east, respectively.

The domain size is 1000 km in x, 150 km in y. The grid spacing is 500 km in x and y, and a stretched grid spacing in z, with 50 m at the surface stretching by log function to 250 m above 5 km. Each simulation is run for 6 hours. The NASA-Goddard version of the LFO scheme (Lin et al. 1983) for single-moment microphysics is used (Schoenberg Ferrier 1994). A 1.5 order turbulent kinetic energy closure is performed using a subgrid mixing scheme according to Deardorff (1980). Surface fluxes of heat and moisture are simulated and the surface layer is based on Monin-Obukhov with Carlon-Boland viscous sub-layer and similarity functions. The soil model used allows for “thermal diffusion” according to MM5/WRF with soil moisture

availability held constant over time. Lower/upper boundary conditions allow for zero flux of vertical diffusion. Rayleigh damping is not used on the lateral boundaries. On the west and east boundaries, open-radiative boundary conditions are applied, while on the south and north boundaries, they are periodic. Finally, the bottom and top used free-slip boundary conditions. Coriolis is turned off, for ease of interpretation of final results.

Convection is initiated at model start time using warm and cold perturbations. Both storms are initiated at the same time. For the supercell, we used a 4-K ellipsoidal warm bubble centered at 1.4-km AGL with a 10-km horizontal radius and a 1.4-km vertical radius that developed into a right-moving supercell after twenty minutes of simulation time. For the squall line, we used a latitudinally homogeneous surface -14-K cold perturbation with a depth of 3.5-km that developed into an eastward-moving squall line. Random temperature perturbations of 0.2 K were added to the cold perturbation to generate 3-D structure in the line.

The models output data every 5 minutes. The data analyzed included: precipitation, vorticity, wind, radar reflectivity, buoyancy, potential temperature, pressure, updraft helicity, and rainwater. These fields were run through scripts to generate the CAPE, CIN, LFC, vertical accelerations, buoyancy pressure, dynamic pressure, and nonlinear pressure fields. The simulations were run using the NCAR Cheyenne Supercomputer.

3.2 Dynamic Analysis

Our numerical model generates necessary data, which we use to compute additional quantities. These quantities, like vertical accelerations (total, buoyant, and dynamic) and pressure (buoyant and dynamic) are useful for performing a more detailed analysis of storm processes.

First, the equations of motion are put into the flux form:

$$\frac{\partial}{\partial t}(\rho_0 \mathbf{u}) = \nabla \cdot (\rho_0 \mathbf{u} \mathbf{u}) + \nabla p' + 2\rho_0 \Omega \times \mathbf{u} - \rho_0 \mathbf{B} = 0 \quad (3.1)$$

where ρ_0 is the density, \mathbf{u} is the wind vector, p' is the perturbation pressure, and Ω is the angular velocity of the Earth. After taking $\nabla \cdot$ (1) this becomes the diagnostic pressure equation:

$$\nabla^2 p' = -\nabla \cdot [\rho_0 (\mathbf{u} \cdot \nabla) \mathbf{u}] + \frac{\partial}{\partial z} (\rho_0 B) \quad (3.2)$$

which is decomposed into buoyant and dynamic components ($p' = p'_B + p'_D$):

$$\nabla^2 p'_B = \frac{\partial}{\partial z} (\rho_0 B) \quad (3.3)$$

$$\nabla^2 p'_D = -\rho_0 [(\frac{\partial \mathbf{u}}{\partial x})^2 + (\frac{\partial \mathbf{v}}{\partial y})^2 + (\frac{\partial \mathbf{w}}{\partial z})^2 - w^2 \frac{\partial^2}{\partial z^2} (\ln \rho_0)] \quad (3.4)$$

where \mathbf{u} , \mathbf{v} , and \mathbf{w} are the horizontal and vertical components of \mathbf{u} , p'_B is the buoyant perturbation pressure, and p'_D is the dynamic perturbation pressure. p_D is high in areas of divergence and deformation, low in areas of rotation. It is composed of a linear part:

$$\nabla^2 p'_{DL} = -2\rho_0 \frac{du_0}{dz} \frac{\partial w}{\partial x} \quad (3.5)$$

and a non-linear part:

$$p'_{DNL} = p'_D - p'_{DL} \quad (3.6)$$

The pressure decomposition gives the equation of motion:

$$\frac{D\mathbf{u}}{Dt} = -\frac{1}{\rho_0} \nabla p'_B - \mathbf{g}(\frac{\rho'_{gas}}{\rho_0}) - \mathbf{g}q_h - \frac{1}{\rho_0} \nabla p'_{DL} - \frac{1}{\rho_0} \nabla p'_{DNL} \quad (3.7)$$

which can be used to determine the respective roles of buoyancy and dynamic effects on accelerations within the storm (Parker and Johnson 2004).

Buoyant forcings occur due to buoyancy and indicate that thermal differences are responsible for changes in motion. One would expect buoyant forcings to be positive in a storm's inflow and updraft and negative in a storm's cold pool. Dynamic forcings occur due to the motion of fluid. One would expect dynamic forcings to be positive at the head of a gust front, where convergence forces air upward. These forcings should also be positive inside a mesocyclone, where high rotation lowers dynamic pressure and accelerates air towards it. Altogether, both sources of acceleration are used to analyze the evolution of the updrafts in the respective supercells.

In the next section, we lay out the results of these simulations, beginning with the COMBINED-SHADED supercell.

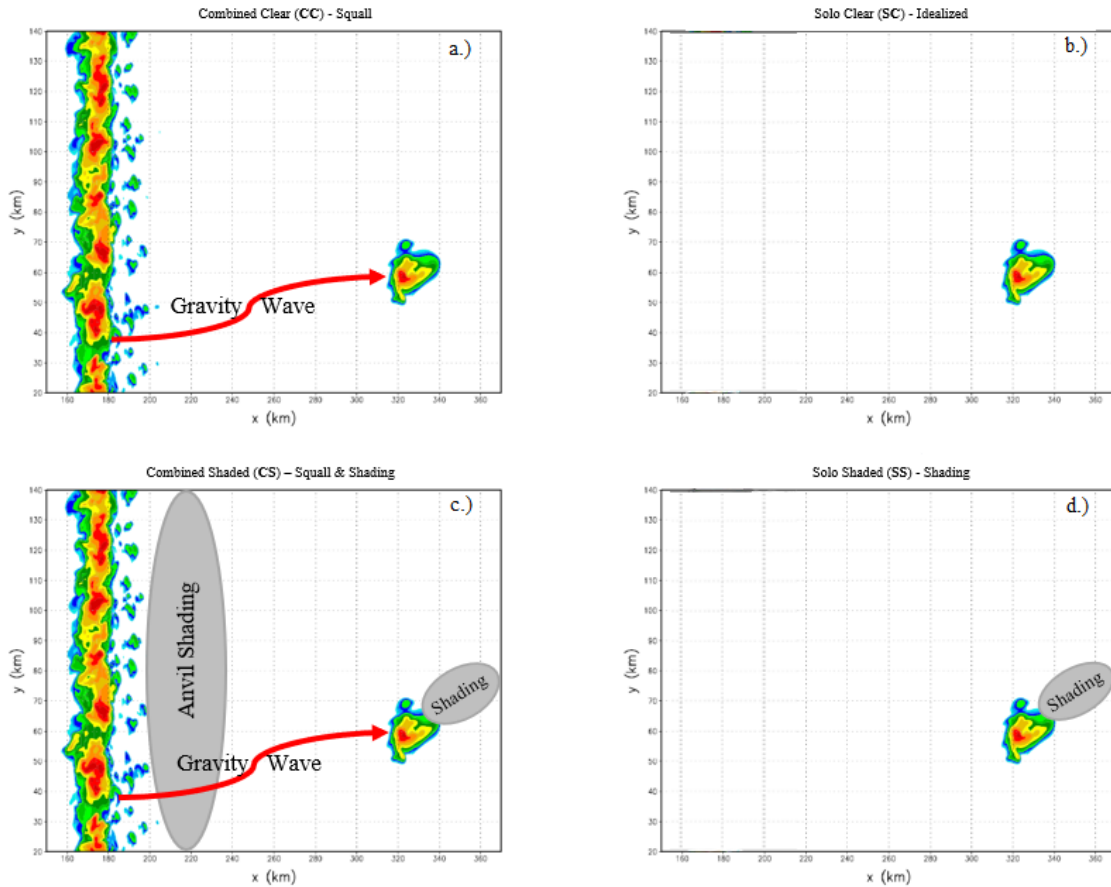


Figure 3.1: Four simulations are presented: a) Combined-Clear (CC), b) Solo-Clear (SC), c) Combined-Shaded (CS), and d) Solo-Shaded (SS). The squall line induced gravity wave is represented by the red curved arrow in a) and c). Anvil shading is represented by gray ovals in c) and d).

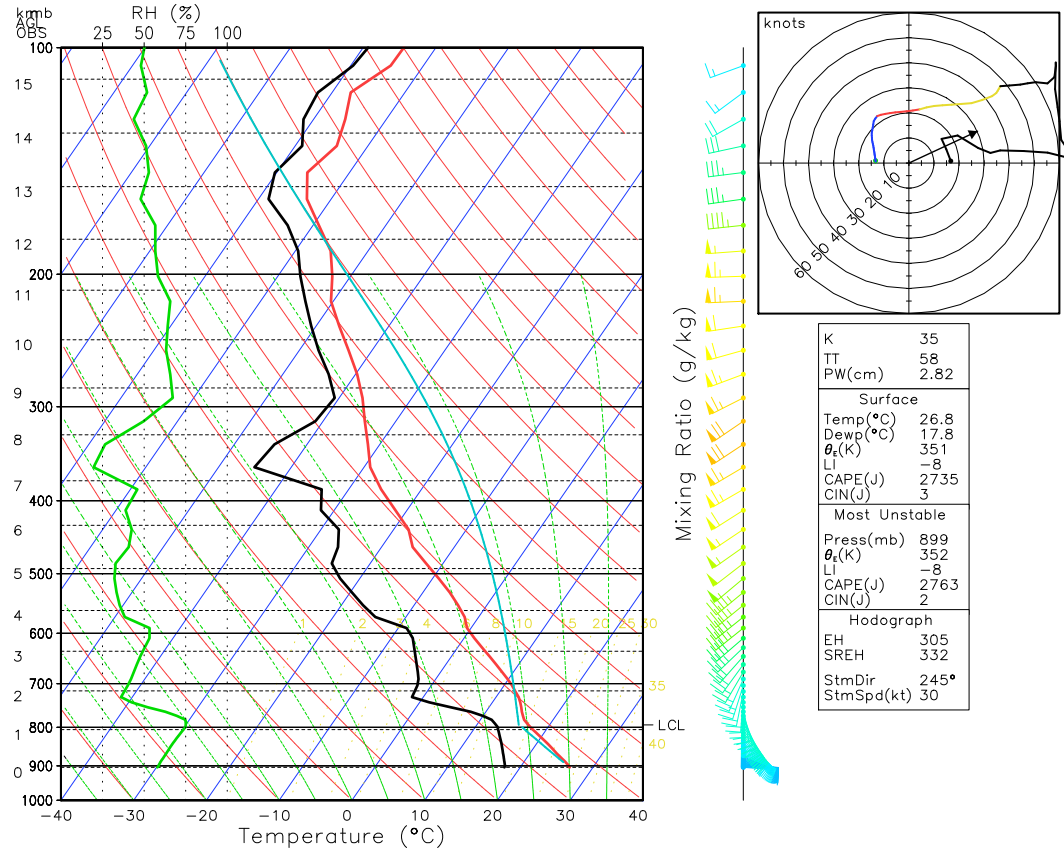


Figure 3.2: Skew-T log-p diagram and hodograph for the 00 UTC sounding from May 24th, 2008 in the Dodge City, Kansas area.

This sounding provides the initial homogeneous base state for all simulations.

Chapter 4

Results

4.1 Overview of combined-shaded simulation

In this section, we lay out the general evolution of the COMBINED-SHADED simulation. It is the most complicated simulation, as it contains both an approaching squall line and anvil shading, and we use it here to illustrate the various components of our experiment. Therefore, we address this case separately from the others. Our goal in this section is to acquaint the reader with how the storms look in the model, how the squall line interacts with its environment, and how anvil shading affects the surface layer. Detailed analysis of the process related to these features will follow in subsequent sections.

4.1.1 Overall storm evolution

In Figure 4.1, we show simulated radar of both the squall line and the supercell at 90 minute intervals, showing the storms initially before interaction (Figure 4.1.a), in pre-merger stage (Figure 4.1.b), and finally when the storms merge (Figure 4.1.c). We see from the first panel the geometry of the simulation, with a latitudinally homogeneous squall line over 100 km west of mature discrete supercell. As the simulation evolves, the squall line continues moving eastward towards the northeastward-moving supercell. Finally, after 5 hr, the squall line overtakes the supercell and merges, which is when the two precipitation fields overly one another. We will focus next on how the squall line affects the environment of the supercell.

4.1.2 Gravity wave

Previous research has shown that squall lines perturb their upstream environment via low-frequency gravity waves (Fovell 2002). Their passage changes multiple fields, beginning with downward motions in the upper atmosphere. As air is forced downward towards the surface,

adiabatic compression heats midlevel air. In this section, we detail the qualities of the gravity wave in our model.

Downward motions are shown in Figure 4.2. This is a Hovmoller diagram, plots used to show how a field evolves in time and a single spatial dimension. There are centers of upward velocity initially at $x = 75$ km and $x = 250$ km, showing the updrafts of the squall line and supercell, respectively. As time increases along the y-axis, these updrafts move eastward. Beginning at 45 minutes, we see a mass of downward motion forming eastward of the squall line's updraft. Tracing a sharp eastward path towards the supercell, the sinking motion moves quickly upstream.

Air in this layer is adiabatically compressed, resulting in midlevel warming (figure 4.3). Mainly residing in the 5 - 7.5 km AGL layer, it extends eastward towards the supercell. Temperatures rise by over 2 K in a layer of air at least 2 km thick (figure 4.4.b) and move eastward towards the supercell (Figure 4.3.c).

The gravity wave raises temperatures while reducing vertical motions, thereby altering the environment. It is coincident with the supercell between 100 and 135 minutes. During this period, the two may interact. This will be discussed in more detail later.

4.1.3 Anvil shading

The other major mechanism for environmental modifications is shading by the respective storm's cirrus anvil. After 30 minutes, the supercell develops an anvil, which spreads eastward and shades the land ahead. As anvil shading cools the ground, vertical eddies form less readily and surface air is restricted from mixing with faster winds aloft. Over time, this results in a cooler inflow environment with less kinetic energy. Figure 4.4 shows how the surface temperature of inflow air changes over time. Initially, only the cold pool of the supercell is visible (Figure 4.4.a). This cold pool continues moving eastward into a rapidly cooling inflow layer (Figure 4.4.b). As this continues, the squall line approaches the supercell, shading its inflow as well (Figure 4.4.c).

In total, the supercell in COMBINED-SHADED is influenced by both the gravity wave and anvil shading. Its upper atmosphere is adiabatically compressed by the downward motion associated with the gravity wave. This warms the upper atmosphere as well. As both of these effects are traveling eastward towards the supercell aloft, the supercell's immediate environment is being cooled near the surface. Each of these effects impacts the supercell's environment in ways that may influence storm dynamics. The next section focuses on how these differences impact storm evolution.

4.2 Overview and comparisons between supercells

With our four simulations, we experiment with increasing layers of complexity. SOLO-CLEAR undergoes no environmental perturbations, while COMBINED-CLEAR and SOLO-SHADED are modified by just one of the two modes. COMBINED-SHADED is modified by both the gravity wave and anvil shading. Despite substantial difference in terms of model configuration, each simulation creates an identical supercell at the start.

After 1 hour, every storm has evolved into a classic supercell (Figure 4.5.a,d,g,i). A deep mesocyclone resides on the southeastern edge of the radar image (black contour). Westward of the mesocyclone is the hook echo, which is the curvature at $x=-8, y=-8$. Northward of the hook echo is the hail core, seen as a maximum in reflectivity. To the northwest stretches more diffuse precipitation, forming the forward-flank precipitation shield. However, these similarities disappear as each evolves uniquely according to their model configurations.

COMBINED-CLEAR evolves over the next 90 minutes into a slightly weaker storm (Figure 4.5.b). While still a supercell, its precipitation covers less area with its forward-flank precipitation shield less extensive. Yet, 90 minutes later, rather than contracting, it has grown and intensified. Nearly doubling its original size and with multiple cores above 50 dbz, at 4 hours it has transitioned into a high-precipitation supercell (Figure 4.5.c).

In contrast, SOLO-CLEAR strengthens continually throughout its lifetime. At 2.5 hours, the storm has grown in size and intensity, as evidenced by the greater area of reflectivity above

50 dbz. By 4 hours, the storm has taken on the shape of a high-precipitation supercell, with an extensive mesocyclone (Figure 4.5.d.-f).

The pattern of COMBINED-SHADED is one of continual weakening. Like COMBINED-CLEAR, its precipitation is less intense and widespread at 2.5 hours. However, in contrast to COMBINED-CLEAR, the storm does not intensify over the next 90 minutes. By 4 hours, the storm has continued weakening, as it is now 1/4th its original size (Figure 4.5.g.-i).

SOLO-SHADED intensifies so that, by 2.5 hours, its reflectivity is more intense and widespread, much like SOLO-CLEAR. In contrast, it does not intensify between 2.5 and 4 hours. While still a steady supercell, its reflectivity has plateaued. Ultimately, SOLO-SHADED is marked by an initially intensification that ultimately is not sustained (Figure 4.5.j.-i).

The simulations diverge in their outcomes based on model configuration. In SOLO-CLEAR, the storm evolves into a powerful, long-lived supercell. Add anvil shading and the storm turns out to be slightly weaker (SOLO-SHADED). With an approaching squall line, the supercell weakens briefly before recovering entirely (COMBINED-CLEAR). When both anvil shading and a squall line are present, the supercell weakens entirely (COMBINED-SHADED). In order to dissect how these changes occur, we next focus on metrics of storm intensity.

One such metric is total upward mass flux, which measures the rate at which inflowing air rises upward through a storm's updraft. This is defined as $F_q = w\Sigma(q_i)$, where q_i refers to cloud water, rainwater, ice, graupel, and water vapor (Figure 4.6.a). We see that both COMBINED-SHADED and COMBINED-CLEAR begin weakening at 100 and 105 minutes, respectively. Over a period of 30 minutes, the storms eventually fall to nearly 50% their former intensity. During this period, neither SOLO simulation weakens.

At 135 minutes, COMBINED-CLEAR begins to recover and eventually grows as strong as SOLO-CLEAR. Meanwhile, COMBINED-SHADED continues weakening. Additionally, despite SOLO-SHADED initially matching the intensity of SOLO-CLEAR, it weakens at 180 minutes. However, it never weakens nearly as much as COMBINED-SHADED.

While F_q illustrates storm growth, supercell research is largely concerned with tornadoes. Our model resolution is too coarse to directly resolve such vortices, so we use low-level vertical vorticity to indicate the strength of near-surface rotation. The metric we use is maximum vertical vorticity below 1 km (figure 4.6.b). Again, all storms are initially similar. However, after 100 minutes, the maximum low-level vertical vorticity is much lower in COMBINED-SHADED than in any other simulation. While the others generate values above 0.03 s^{-1} , COMBINED-SHADED never rises above 0.02 s^{-1} . Even though both COMBINED-CLEAR and COMBINED-SHADED undergo significant weakening, near-surface vortices decline in COMBINED-SHADED alone. Additionally, the differing responses in terms of vertical vorticity indicates that, despite substantial losses in F_q , COMBINED-CLEAR never truly weakens since it's as likely as SOLO-CLEAR to produce a dangerous tornado.

Returning to the updraft again, Figure 4.6.c-d show the maximum updraft speed at different levels. Both COMBINED updrafts weaken in the midlevels at 115 minutes to a similar degree (Figure 4.6.c). In contrast, the low-level updraft responds differently, with COMBINED-CLEAR maintaining similar strength to the SOLO runs while COMBINED-SHADED weakens (Figure 4.6.d).

Here, we see that initially the flux of both COMBINED supercells weakens at 100 minutes. However, these similarities disappear after 135 minutes, when COMBINED-CLEAR recovers completely and COMBINED-SHADED continues to weaken. We also note that the low-level vertical vorticity declines only in COMBINED-SHADED. Additionally, although in both COMBINED simulations the midlevel updrafts are similarly affected, only in COMBINED-SHADED is the low-level updraft is affected. Altogether, this analysis shows that COMBINED-CLEAR and COMBINED-SHADED initially act alike, but respond differently after 135 minutes. The following analysis focuses on the mechanisms causing these differences.

4.3 Relation between observed behavior and hypothesized mechanisms

The previous section showed that storm behavior depends on model configuration. In this section, we investigate these dependencies and propose physical mechanisms that link storm behavior with model configuration.

The COMBINED simulations deviate from the SOLO runs, as they weaken at 105 minutes while the SOLO runs continue to grow. The weakening is nearly identical between COMBINED-SHADED and COMBINED-CLEAR, implying that the weakening is in response to the approaching squall line. Well before the squall line directly merges with the supercell, it generates a gravity wave that intercepts the supercell between 100 and 140 minutes. The timing implicates the gravity wave as a source of the observed supercell weakening, as this is the same time period during which both COMBINED simulations weaken. It is not well understood how gravity waves may interact with supercells, yet in our opinion there are two possibilities: direct interactions or indirect interactions.

It is well established that gravity wave passage alters the environment, generating heating and downward motion (Fovell 2002). Such changes may modify the fields necessary to sustain convection. Specifically, midtropospheric heating may weaken the buoyancy of surface parcels, thereby inhibiting their upward movement. This would reduce convective available potential energy (CAPE), which is critical for convection. Additionally, the gravity wave can alter the local wind field, which could affect the vertical wind shear. If the 0 - 6 km AGL bulk wind shear (BWD06) were suddenly reduced, one would expect supercells to become disorganized. In these ways, the gravity wave may act as a second order effect on the supercell, weakening it by altering its environment.

In the other case, the gravity wave may directly impact the supercell. While far less studied, such internal interactions are possible (e.g. Coleman and Knupp 2008). As the sinking motion moves through the supercell, the storm's updraft could be affected in any number of ways. The most obvious of which would be simple subtraction of vertical velocity, which would weaken the updraft. There could also be more complex interactions, whereby the quickly mov-

ing mass of air impinges on the updraft, possibly generating unfavorable pressure gradients. Lastly, midtropospheric heating may alter the buoyancy of the updraft. This is slightly different than lowering CAPE at the surface, instead it could disorganize the updraft by increasing its surrounding temperature. Past studies have not studied such effects. However, if indirect interactions were ruled out, the only other explanation would be that the gravity wave directly alters the structure of the storm itself.

Once weakened, the COMBINED storms react differently based on whether or not there is anvil shading. COMBINED-CLEAR reverses its declining F_q at 135 minutes, and afterwards goes on unencumbered, while COMBINED-SHADED never fully recovers. Its presence mediates whether or not a storm can recover. Previous studies, completed by Frame and Markowski (2013), also found that supercells were weaker when there was anvil shading. As the shaded ground cooled, surface winds slowed down. The difference between surface winds and 1 km AGL winds increased, thereby enhancing vertical wind shear in the same sense as the cold pool. This upset the balance between the cold pool and the inflow winds, ultimately causing the cold pool to rush out ahead of the updraft. If a similar process were at work in these simulations, one would expect low-level vertical wind shear to be enhanced in COMBINED-SHADED. Additionally, a cooler surface may reduce the buoyancy of surface parcels. This could weaken CAPE which would weaken the supercell.

Thus, three proposed mechanisms exist:

- The gravity wave may act directly on the supercell.
- The gravity wave may alter the environment, making it less conducive to convection.
- The low-level environment can become less conducive to convection due to anvil shading.

In order to determine which mechanisms are at work, we evaluate each in term in the next section.

4.4 Evaluation of hypothesized mechanisms

4.4.1 Role of gravity wave and anvil-shading induced environmental changes

If indirect effects were responsible for observed storm behavior, the weakened storms should have significant deficiencies in their environmental parameters. Our analysis focuses on how CAPE and vertical wind shear evolve in each simulation.

Figure 4.7.a, shows the average CAPE for the supercell inflow environment, which is 20 km E of the storm. Initially, clear CAPE is 200 J kg^{-1} higher than shaded CAPE. After 140 minutes, the CAPE of the COMBINED simulations becomes nearly identical, just as does the CAPE of SOLO simulations. While CAPE does differ for each simulation, values vary by as little as $200 - 400 \text{ J kg}^{-1}$. The maximum vertical velocity can be related to CAPE by the following empirical formula (Markowski and Richardson 2010):

$$w_{max} = \sqrt{2CAPE} \quad (4.1)$$

The largest variation in CAPE is 400 J kg^{-1} . This yields a difference of 4 m/s , which is too insignificant to affect storm behavior. Moreover, all environments contain at least the minimum 1500 J kg^{-1} of CAPE, which is sufficient for supercells. Therefore, changes in CAPE are likely not the driving factors in the observed storm behavior.

Storm structure is also dependent on deep-layer shear, which is the difference between winds at 0 km AGL and 6 km AGL, often referred to as the 0-6 km Bulk Wind-vector Difference (BWD06):

$$\vec{V}_{Shr} = \vec{V}_{6km} - \vec{V}_{sfc}. \quad (4.2)$$

Supercells require BWD06 $> 20 \text{ m/s}$, otherwise storm rotation and updraft strength would diminish (Weisman and Rotunno 1983). Figure 4.7.b shows that all simulations contain similar values of BWD06, different by at most 3 m/s . At 160 minutes, BWD06 falls for the COMBINED simulations, but again resulting in only negligible differences. BWD06 remains well above the necessary 20 m/s in all simulations.

Neither CAPE nor BWD06 change in any way that could negatively affect the supercells. However, anvil shading modifies the environment as well, introducing additional effects. Changes principally happen through radiative cooling. Indeed, figure 4.7.a shows that the inflow of shaded simulations is 1 K colder at 2 hours. This could reduce CAPE, but, of course, no such changes were observed. Theoretically, lower surface temperatures should reduce vertical mixing. Slower surface winds should mix less with high-velocity winds aloft, thus enhancing low-level vertical wind shear in shaded simulations. However, figure 4.7.d shows no such trends. SOLO-CLEAR and SOLO-SHADED maintain similar values. Likewise, COMBINED-CLEAR and COMBINED-SHADED are identical until 160 minutes, when shear becomes higher in COMBINED-CLEAR. This is the opposite of the expected trend. In contrast to the results of Frame and Markowski (2013) (FM13), low-level vertical wind shear for shaded simulations is not enhanced.

Altogether, environmental differences are negligible, as all simulations possess sufficient CAPE and vertical wind shear to maintain supercell storms. However, despite these favorable conditions, the COMBINED supercells weaken, and later, when COMBINED-CLEAR recovers, its environment is similar to that of COMBINED-SHADED. Therefore, the COMBINED storms do not behave differently because of an altered environment. Without such indirect interactions, it is likely that the gravity wave and anvil shading interact with the supercell directly.

4.4.2 Role of direct influence of gravity wave on supercell's midlevel updraft

As stated earlier, little research exists concerning the relationship between gravity waves and mesocyclones. Coleman and Knupp (2008) identified one possible mechanism, in which gravity waves could increase or decrease vertical vorticity within a supercell's mesocyclone. However, in our simulations, the vertical vorticity of COMBINED mesocyclones aloft is similar to that of SOLO mesocyclones aloft (not shown). We therefore infer a different mechanism. The gravity wave acts directly on the supercell by heating air surrounding the mesocyclone, disrupting the careful balance of buoyancy and thereby weakening upward accelerations.

The following analysis will show first how each midlevel updraft evolves during the period 115 to 155 minutes, covering the full transition from healthy storm to recover/decay. After that, we explore the accelerations underlying these changes.

First, we examine the midlevel updrafts, at 7 km AGL. At the start, the updrafts are nearly indistinguishable, all of them powerful with upward velocities over 50 m/s . Differences emerge over the next 20 minutes. While the SOLO simulations grow unimpeded, the COMBINED updrafts weaken in both speed and size (Figure 4.8.b and 4.8.h). There is a clear sign of weakening in both COMBINED storms at 135 minutes. Thereafter, the simulations diverge, as COMBINED-CLEAR recovers its updraft entirely (Figure 4.8.c) while COMBINED-SHADED continues to decay (Figure 4.8.i).

Meanwhile, both SOLO updrafts intensify during this period. At 135 minutes, new mesocyclones appear in SOLO-CLEAR (Figure 4.8.e) and SOLO-SHADED (Figure 4.8.k). Both are favorably positioned on the inflow notch, close to moist, buoyant inflow air, which leads to continued strength at 155 minutes (Figure 4.8.f,l).

Each updraft evolves according to internal forcings. Dynamic and buoyant forces determine the storm's total accelerations, which control the evolution of each updraft. In Figure 4.9, we show how each updraft responds to these forcings. At 115 minutes, all updrafts are strong and deep, with upward velocities over 45 m/s and positive accelerations reaching upward to at least 8 km AGL (Figure 4.9.a,d,g,j). At 135 minutes, a horizontal line of negative total accelerations appears at the midlevels, cutting off the low-level updraft from the upper-level updraft in both COMBINED simulations (Figure 4.9.b,h). Both SOLO simulations maintain large layers of positive (upward) accelerations throughout this time (Figure 4.9.e,k).

These negative total accelerations arise principally through buoyant accelerations (Figure 4.10). Before the updrafts weaken, we see at 115 minutes that a region of negative buoyant accelerations appears in both COMBINED simulations (Figure 4.10.a,g at ($x = -4$ to 0, $z = 8$ to 12)). It moves downward over the next 20 minutes so that, at 135 minutes, it has relocated to the midlevels (Figure 4.10.b,h ($z = 5$ to 6, $x = -3$ to 4)). Its strong similarity to the

negative total accelerations in Figure 4.9.b,h indicates that negative buoyancy perturbations caused COMBINED updrafts to weaken. However, 20 minutes later at 155 minutes, it has mostly disappeared in COMBINED-CLEAR, allowing it to regain its updraft (Figure 4.10.c). Similar improved conditions are in COMBINED-SHADED, but it has not regained its updraft (Figure 4.10.i).

The SOLO simulations are not so overwhelmed by negative buoyancy. During this period, both SOLO simulations experience only slight negative buoyancy, which is surrounded by positive buoyancy (Figure 4.10.e,f,k,l). This favorable balance allows SOLO updrafts to intensify throughout the period.

To explain how COMBINED-CLEAR intensifies while COMBINED-SHADED stagnates, we refer finally to the dynamic accelerations (Figure 4.11). However, whereas before we examined the full transition from 115, 135, to 155 minutes, here we shift our focus to the latter period (135, 145, to 155 minutes), as it allows us to examine the recovery phase in COMBINED-CLEAR and stagnation in COMBINED-SHADED. Initially, both COMBINED runs contain weak dynamic accelerations (Figure 4.11.a,g). Yet, by 145 minutes, positive dynamic accelerations stretch from close to the surface to well above 8 km AGL, but only for COMBINED-CLEAR. COMBINED-SHADED, however, never regains positive dynamic forcings.

Altogether, Figures 4.9,10,11 show why each storm develops different midlevel updrafts. Figure 4.9 shows that negative total accelerations appear in both COMBINED simulations. Figure 4.10 shows that this weakening is caused by deficient buoyant accelerations. This is likely associated with the gravity wave, which warms upper level air and reduces buoyancy aloft. Eventually, this abnormality disappears at 155 minutes, and allows COMBINED-CLEAR to recover. Figure 4.11 explains why there is a “missing recovery” phase in COMBINED-SHADED. It is missing in COMBINED-SHADED because positive dynamic accelerations are missing. In COMBINED-CLEAR, however, dynamic forcings become positive closer to the surface, which implicates the low-level updraft as responsible for its re-intensification. For that reason, we shift our focus to each storm’s low-level updraft.

Next, we examine the low-level updrafts, at 1 km AGL (Figure 4.12). These control the ingestion of moist, buoyant air near the surface. In COMBINED-CLEAR, low-level lift continues throughout the transition. At 135 minutes, there is lifting on the forward-flank convergence boundary (Figure 4.12.b). By 155 minutes, air ascends on both the forward and rear flank (Figure 4.12.c). This rapid intensification of COMBINED-CLEAR’s low-level updraft is in sharp contrast to COMBINED-SHADED, which decays steadily throughout this period. 135 minutes shows a smaller, weaker updraft (Figure 4.12.h). By 155 minutes, vertical velocities in COMBINED-SHADED are less than 50% of earlier values.

While the SOLO low-level updrafts evolve uniquely, both intensify continually from 115 to 155 minutes. The SOLO-CLEAR updraft transforms similarly to COMBINED-CLEAR, with strong lifting along the FFCB at 135 minutes (Figure 4.12.e) which transforms into extraordinary lifting along both flanks at 155 minutes (Figure 4.12.f). While SOLO-SHADED keeps its shape and does not transform, maximum values grow steadily from 11 m/s at 135 minutes (Figure 4.12.k) to well over 12 m/s over more area by 155 minutes (Figure 4.12.l).

Figure 4.8 showed that the COMBINED midlevel updrafts weaken to similar degrees, at first. Then, the storms respond differently depending on whether or not there is anvil shading. Figure 4.12 showed that only the COMBINED-SHADED low-level updraft weakens. COMBINED-CLEAR, on the other hand, retains a strong source of low-level lifting. Its presence allows the midlevel updraft to regenerate at 155 minutes. In COMBINED-SHADED, the disappearance of a low-level updraft eliminates the possibility of a new updraft, essentially cutting off any chance of recovery. Since differences in storm evolution after 135 minutes are likely controlled by the low-level updraft, we shift our focus to the forcings responsible for vertical velocity at 1 km AGL.

We begin with an analysis of the total vertical accelerations at low-levels. The general pattern of vertical accelerations is similar to what was gleaned from Figure 4.12, which showed transformations in CLEAR simulations and weakening in COMBINED-SHADED. The SOLO supercells maintain the highest accelerations, though with different patterns. Whereas SOLO-

SHADED focuses lifting close to the inflow notch (Figure 4.14.l), SOLO-CLEAR contains lifting along both sides of its gust front (Figure 4.14.f). COMBINED-CLEAR, though slightly weaker at 135 minutes (figure 4.14.b), generates intense accelerations by 155 minutes (Figure 4.14.c). On the other hand, COMBINED-SHADED retains only weakly positive accelerations at 135 minutes (Figure 4.14.h) before they disappear entirely at 155 minutes (Figure 4.14.i).

The dynamic accelerations are transient and quickly changing, but figure 4.14 shows that they trend positive in the strong supercells. Though initially confined to the inflow notch, by 135 minutes the dynamical accelerations are positive along the forward flank (Figures 4.14.b, .e, .k). They then refocus along the rear flank (Figures 4.14.c, .f, .l). In contrast, COMBINED-SHADED contains only negative dynamical accelerations, which are first centered on the rear flank (Figure 4.14.h) and then spread along the entire length of the gust front (Figure 4.14.i).

Dynamical accelerations arise due to dynamic pressure perturbations. High pressure forms at the surface, where the cold pools collides with inflow air. Their convergence forces air upward towards the mesocyclone, which is characterized by low perturbation pressure. Figure 4.15 shows how dynamic pressure is distributed along this interface. High pressure exists ahead of the cold pool, low pressure above and behind it. This pattern is present for all but COMBINED-SHADED. Instead, both the high pressure perturbation at the surface and the low pressure perturbation above weaken over time (Figure 4.15.h). Eventually, pressure becomes negative at the surface and positive above (Figure 4.15.i). COMBINED-SHADED evolves a downward directed vertical pressure gradient, which is extremely unfavorable for upward lifting.

The other component that causes lift is buoyant accelerations, which we show in Figure 4.16. Here we see that, though both COMBINED simulations are weaker than both SOLO simulations, COMBINED-SHADED is weakest of all (Figure 4.16.b,e,h,k). While COMBINED-CLEAR transforms into a similar shape to SOLO-CLEAR (Figure 4.16.c,f),

COMBINED-SHADED stagnates in its original shape (Figure 4.16.g,h,i). It also weakens over time. By 155 minutes, COMBINED-SHADED has the weakest and most poorly positioned buoyant accelerations.

Buoyant forcings are controlled by the distribution of buoyant pressure and buoyancy:

$$F_B = -\frac{1}{\rho} \frac{\partial p'_B}{\partial z} + B \quad (4.3)$$

F_B is buoyant forcing, ρ is density, p'_B is buoyant perturbation pressure, and B is buoyancy. In the best circumstances, buoyant inflow lies below a buoyant updraft. This is partly because of highly buoyant inflow, since its high instability makes vertical lifting easier. In Figure 4.17, favorable inflow and updraft buoyancy profiles are present in all but COMBINED-SHADED. In that case, the inflow cools while the updraft retreats rearward of the cold pool (Figure 4.17.h,i). Such a dislocation in COMBINED-SHADED creates only modest upward accelerations.

Buoyancy distributes itself differently based on how each model is configured. The role of anvil shading is revealed by SOLO-SHADED, which shows negative buoyancy in its inflow. While this is somewhat unfavorable, SOLO-SHADED retains a highly buoyant updraft that is positioned above its inflow (Figure 4.17.j, .k, .l). It generates positive buoyant lifting because only its inflow is weakened. Similarly, the balance in COMBINED-CLEAR is weaker at 135 minutes, as its updraft has moved rearward above the cold pool, away from moist, buoyant inflow (Figure 4.17.b). While, again, this is somewhat unfavorable, COMBINED-CLEAR balances this negative effect by retaining positively buoyant inflow. This allows the storm to continue generating buoyant lifting. In COMBINED-SHADED, it suffers both a negatively buoyant inflow and a poorly positioned updraft (Figures 4.17.h and 4.17.i). Together, this causes the storm to be cut off from moist, buoyant inflow.

4.4.3 Role of anvil-shading on “missing” recovery phase in CS

As hinted at earlier, anvil-shading also plays a direct role in the “missing” recovery phase in COMBINED-SHADED. Rather than changing CAPE or vertical wind shear, anvil-shading

modifies the temperature gradient of the gust front. As the thermal difference along the FFCB diminishes, so does dynamical lifting. The two are directly related:

$$w_{CP} \propto \Delta\theta \quad (4.4)$$

w_{CP} is the upward velocity at the cold pool's edge, and $\Delta\theta$ is the temperature gradient along the gust front on the surface.

At 135 minutes, COMBINED-CLEAR retains strong temperature gradients along its FFCB (Figure 4.18.b, $x = 2, y = 1$), which run sharply to the northeast with gradients above 2.5 K/km (Figure 4.18.b). Meanwhile, in COMBINED-SHADED, temperature differentials of just over 1.5 K/km extend only 1.5 km along the FFCB (Figure 4.18.h). By lowering $\Delta\theta$, anvil shading diminishes dynamical lifting along the forward flank convergence boundary.

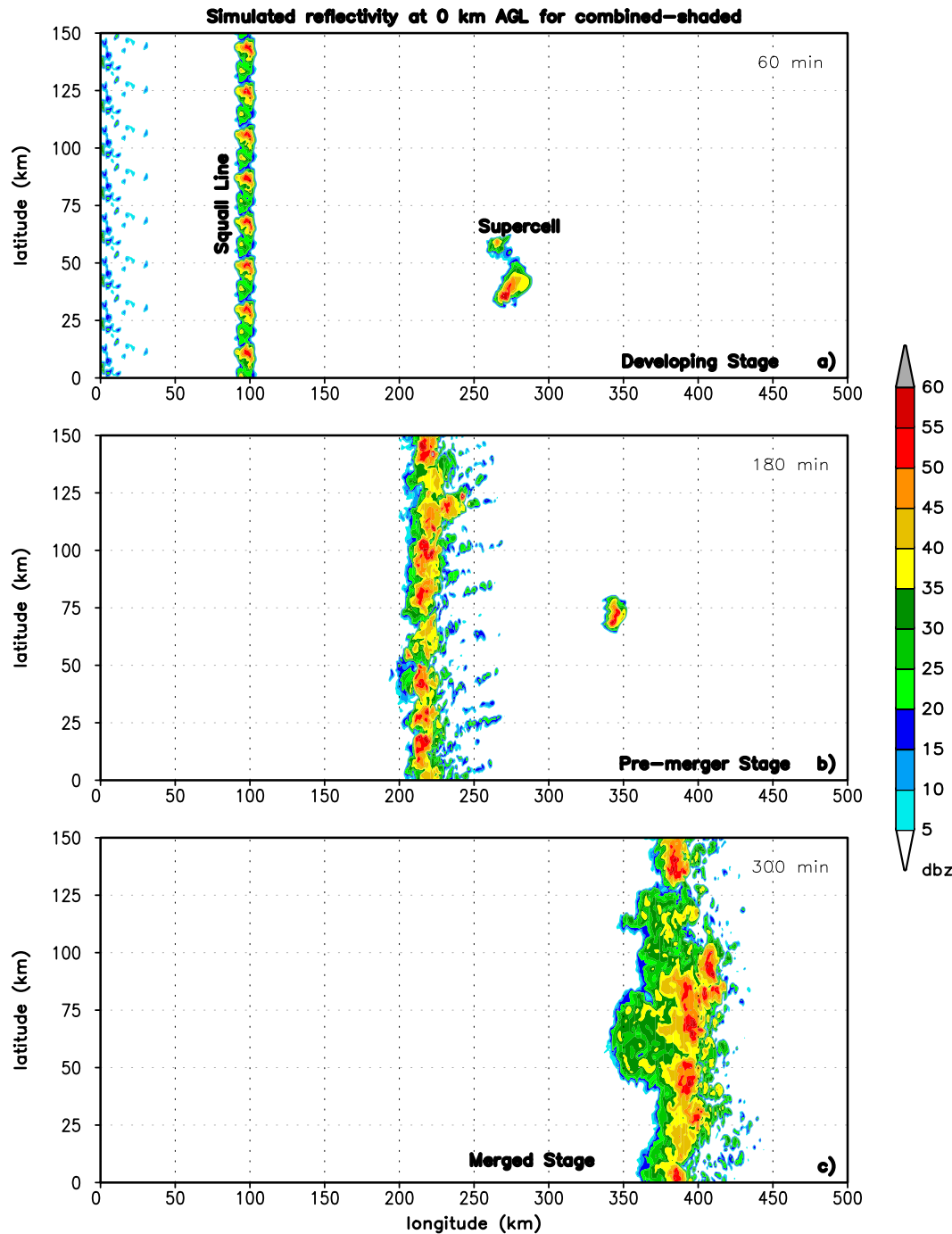


Figure 4.1: Simulated radar reflectivity (dBZ, shaded as shown) for COMBINED-SHADED simulation (top-bottom) $t = 60, 180$, and 300 minutes into the simulation.

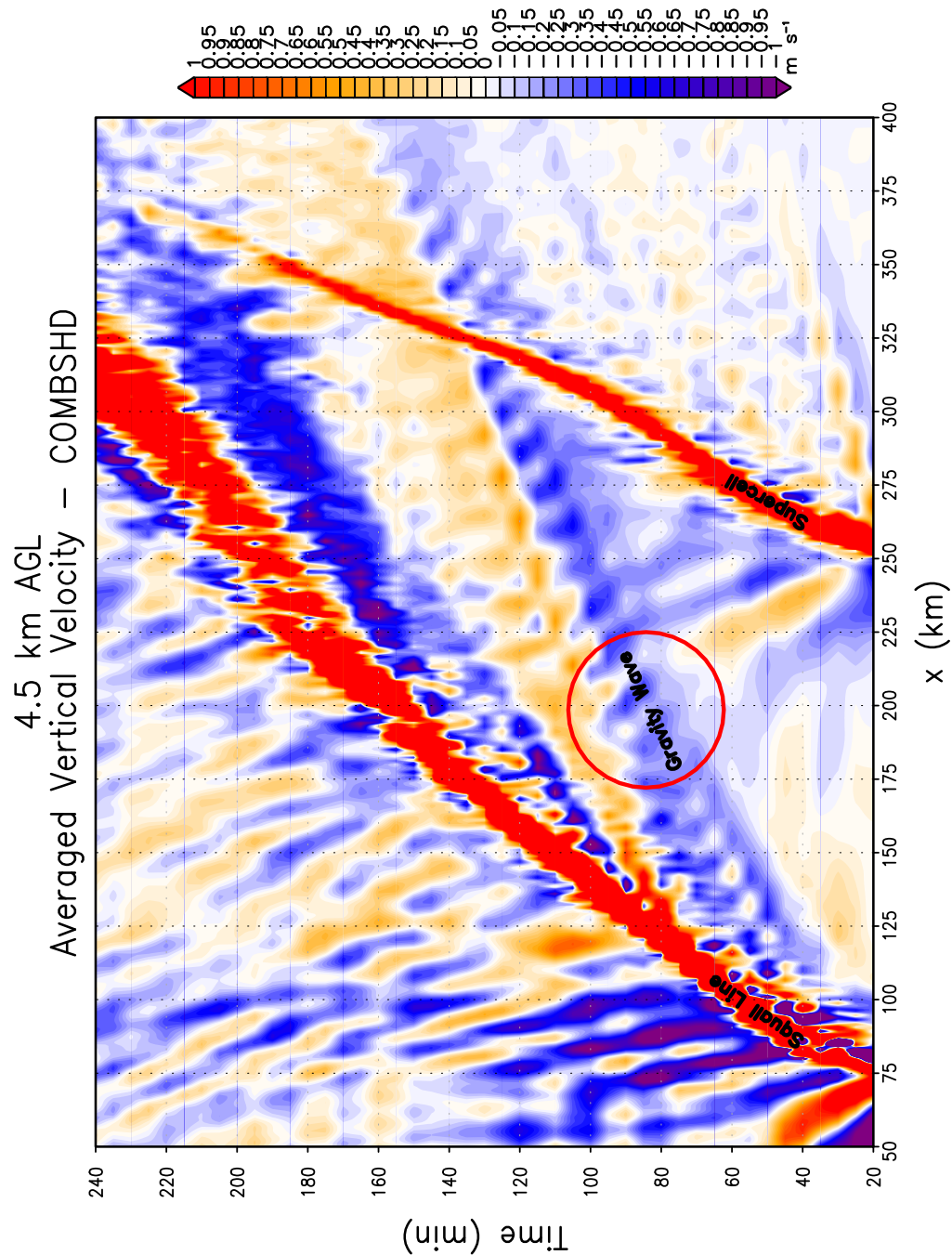


Figure 4.2: Hovmoller (time-longitude) diagram of vertical velocity (shaded as shown, ms^{-1}) averaged domain-wide in the y-direction at 4.5 km AGL.

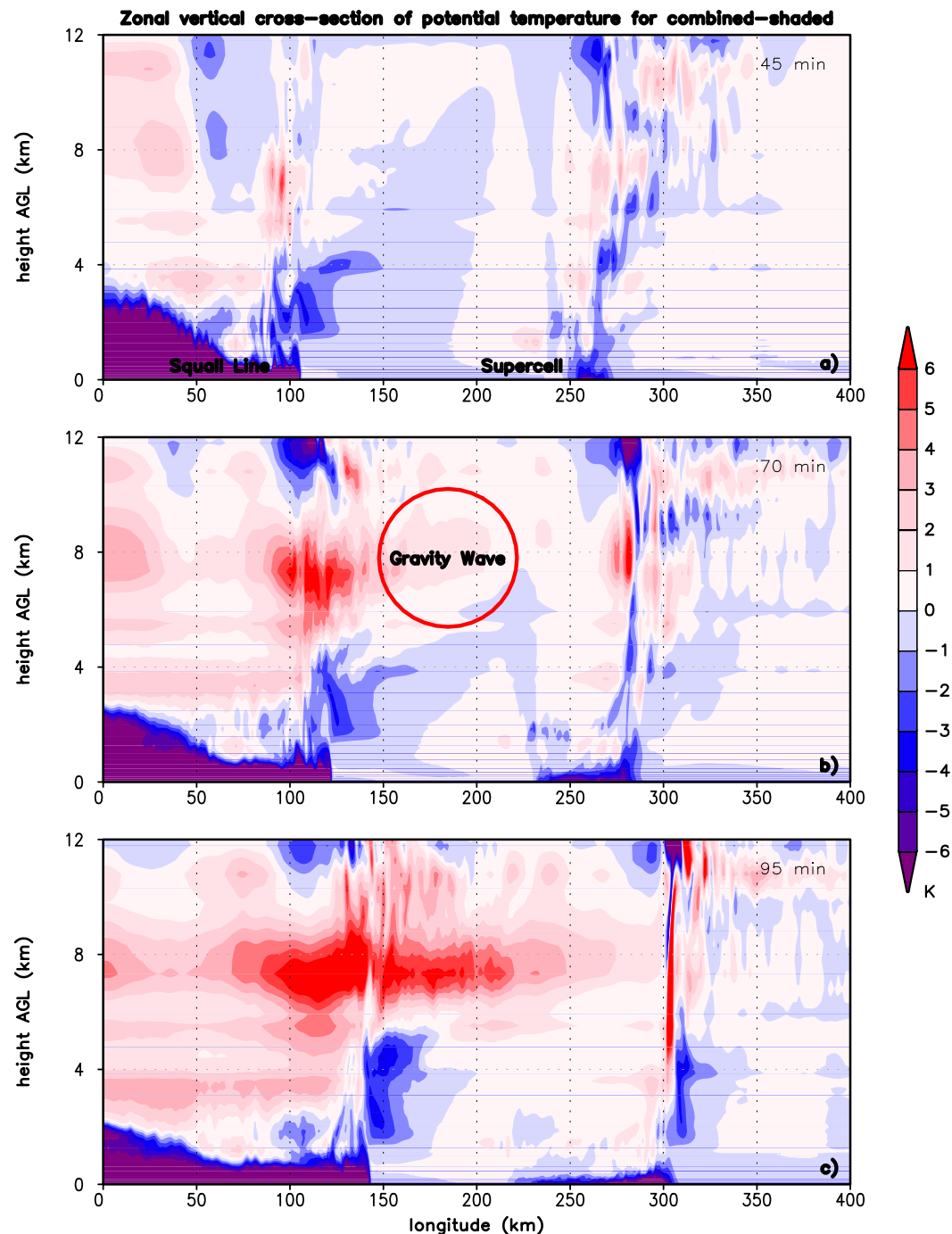


Figure 4.3: Vertical cross-section showing the potential temperature perturbation (K, shaded as shown), for latitude = 44 (since this captures both the supercell and the squall line), averaged 10 km north and south.

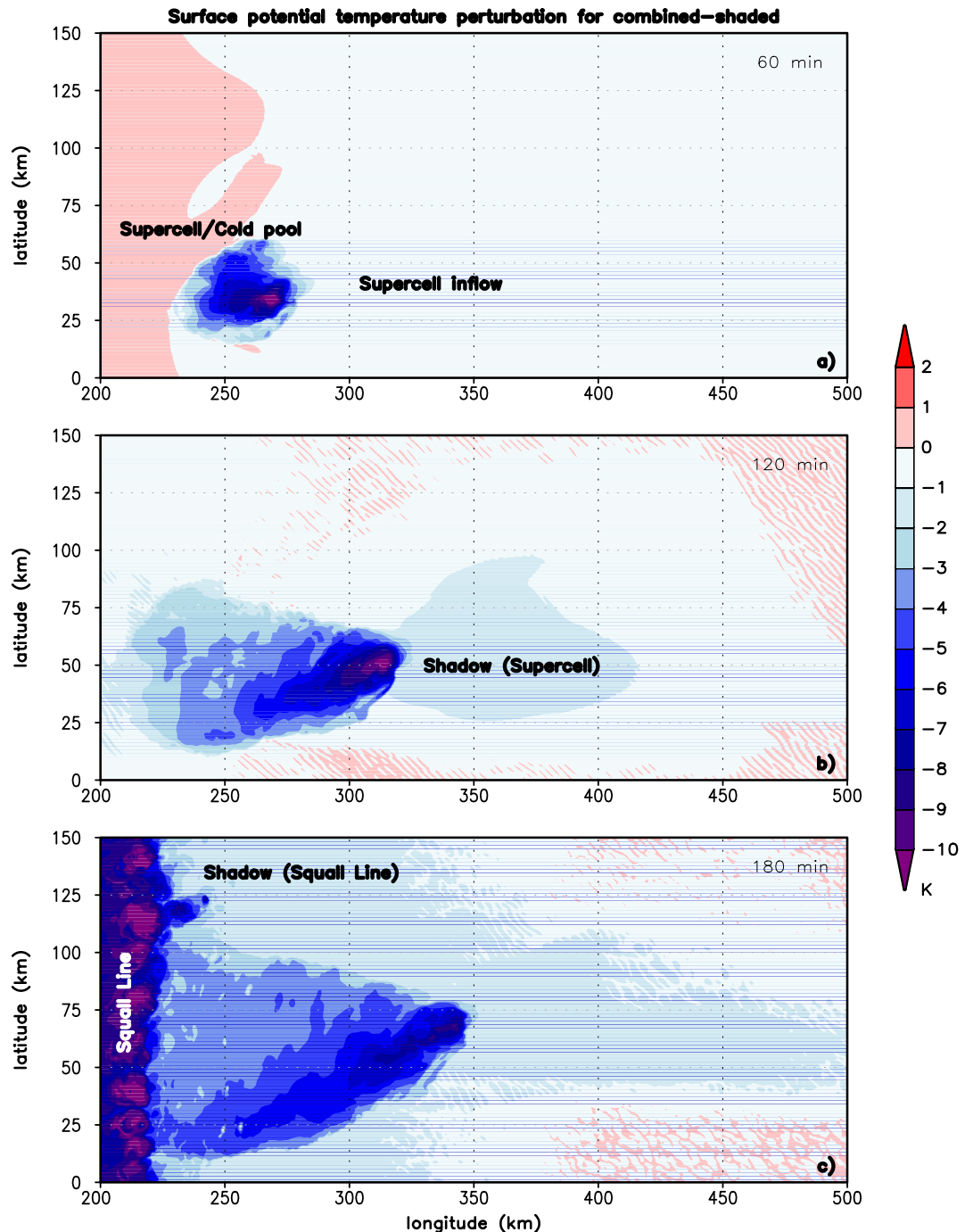


Figure 4.4: Horizontal cross-section at 0 km AGL of potential temperature perturbation (K, shaded as shown).

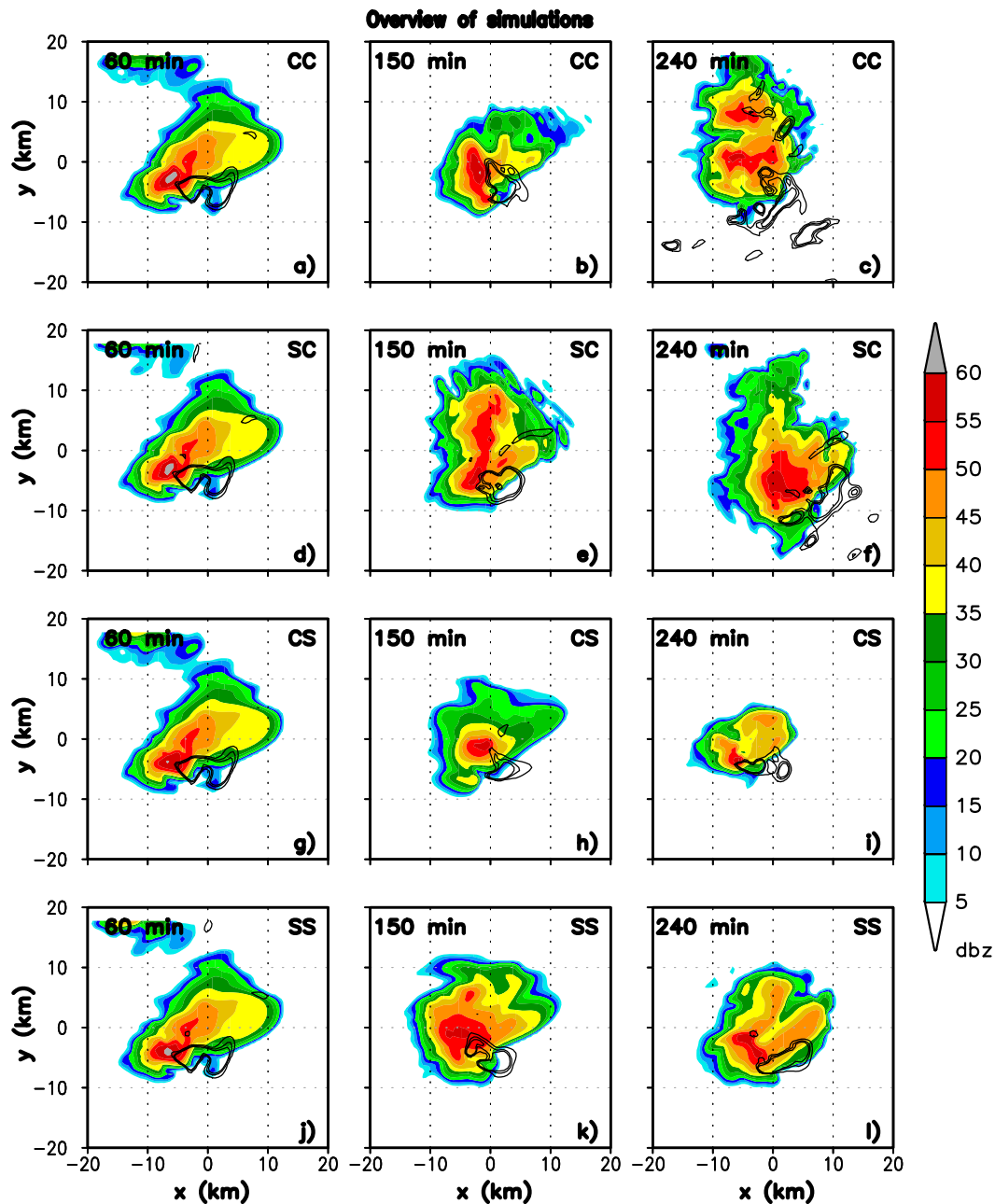


Figure 4.5: Simulated radar reflectivity (dBZ, shaded as shown) and updraft helicity ($m^2 s^{-2}$, contour in intervals of 100, black contours) for (top to bottom) COMBINED-CLEAR, SOLO-CLEAR, COMBINED-SHADED, SOLO-SHADED, at (left to right) $t = 115, 135, 155$ minutes.

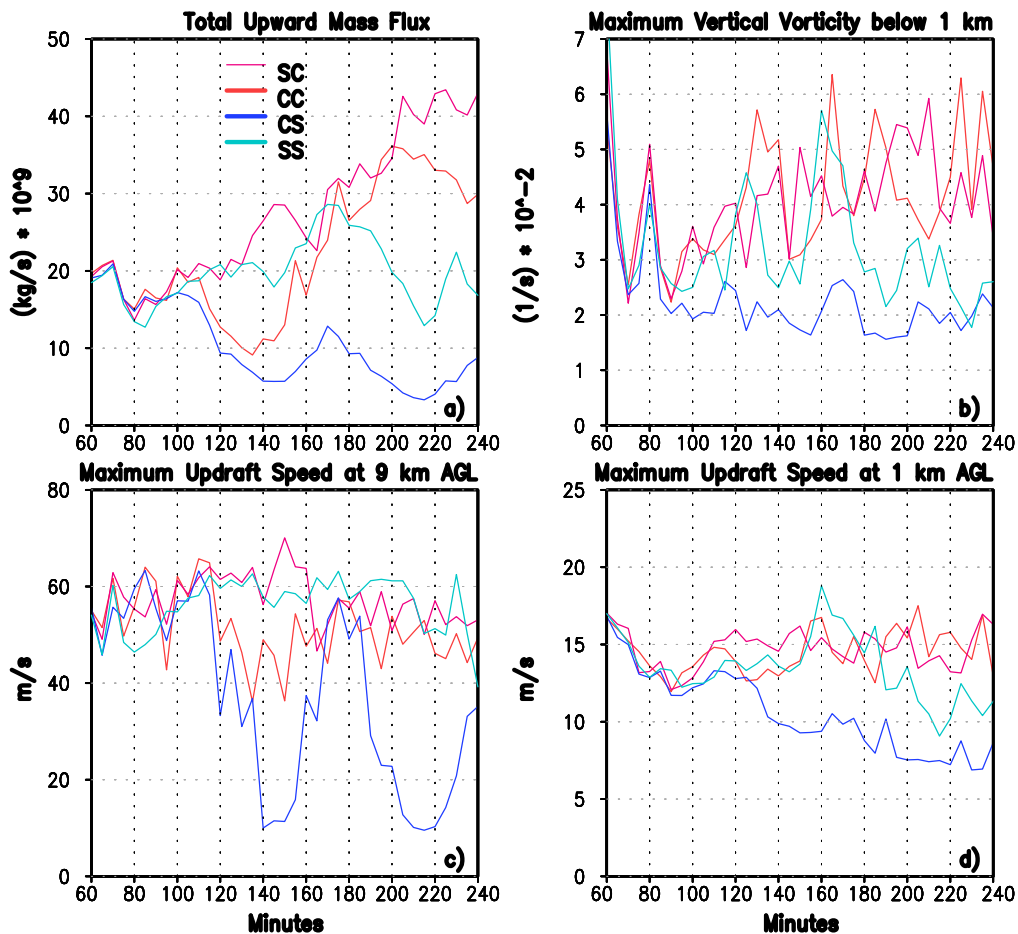


Figure 4.6: Time-series of a) Total upward mass flux, b) Maximum Vertical Vorticity below 1 km AGL, c) Maximum Updraft Speed at 9 km AGL, and d) Area with $w \geq 5 \text{ ms}^{-1}$ at 9 km AGL between $t = 1 \text{ hr}$ and 4 hr of simulation time for COMBINED-CLEAR = red, SOLO-CLEAR = pink, COMBINED-SHADED = blue, SOLO-SHADED = teal.

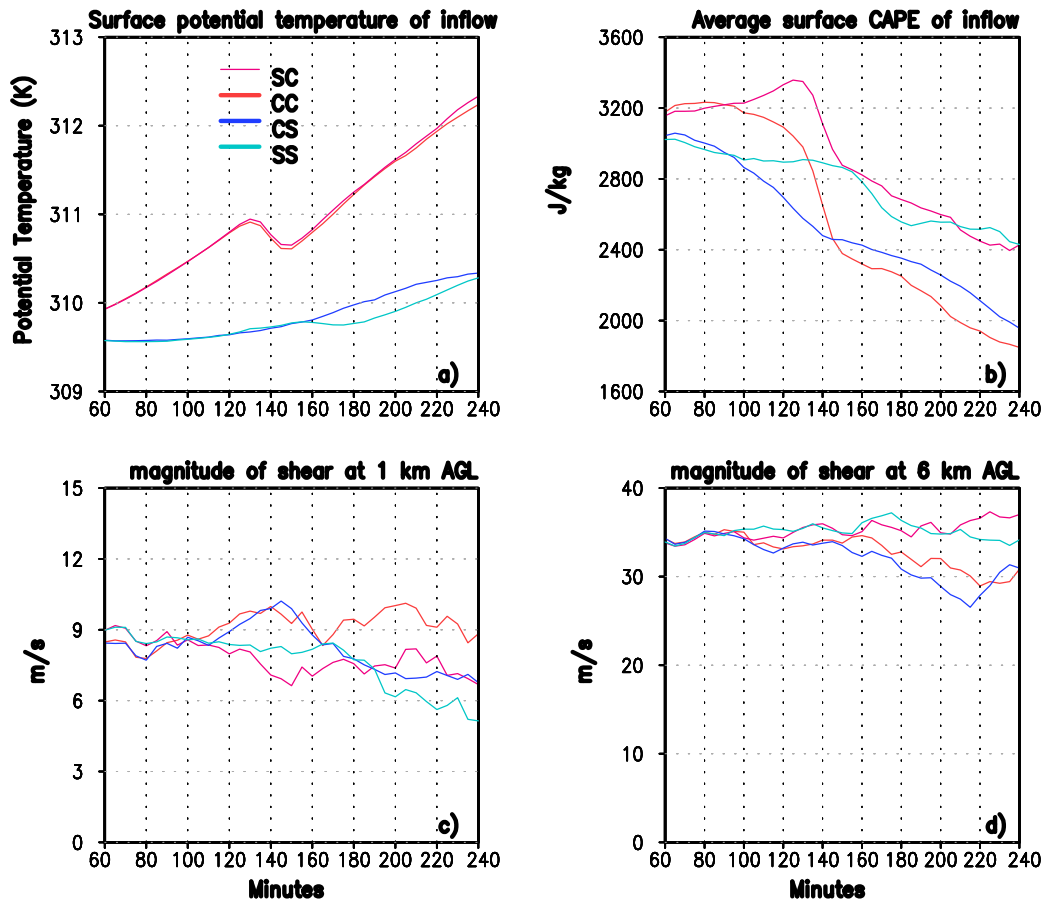


Figure 4.7: Time series of a) Surface potential temperature of inflow, b) average surface CAPE of inflow, c) magnitude of shear at 1 km AGL, and d) magnitude of shear at 6 km AGL between $t = 1$ hr and 4 hr of simulation time for COMBINED-CLEAR = red, SOLO-CLEAR = pink, COMBINED-SHADED = blue, SOLO-SHADED = teal.

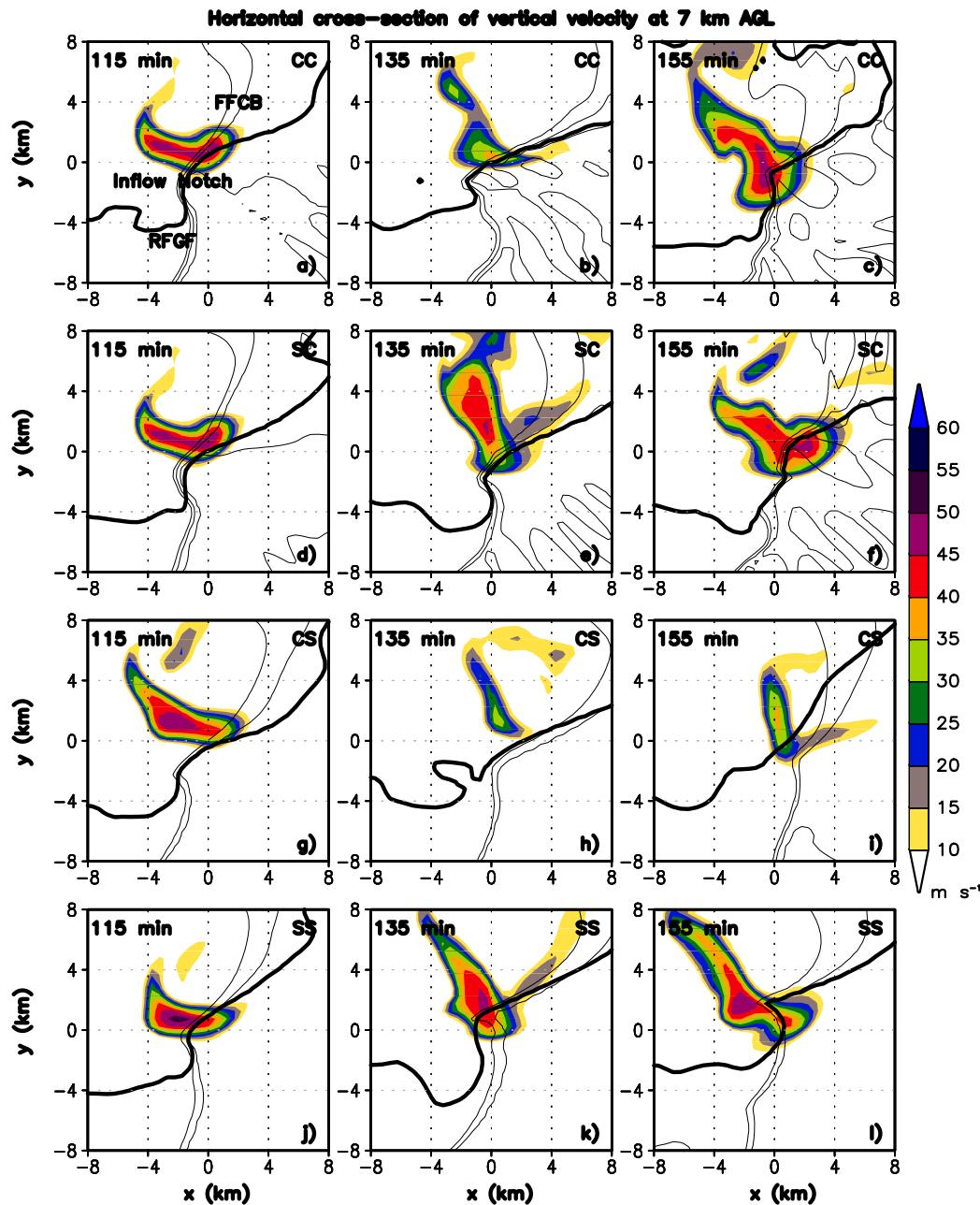


Figure 4.8: Horizontal cross-sections of the 7 km AGL updraft with w (shaded, as shown) and surface perturbation potential temperature (contoured in thin black, -2, -1 0 K) and 15 dBZ (contoured in thick black), at times 115, 135, and 155 minutes.

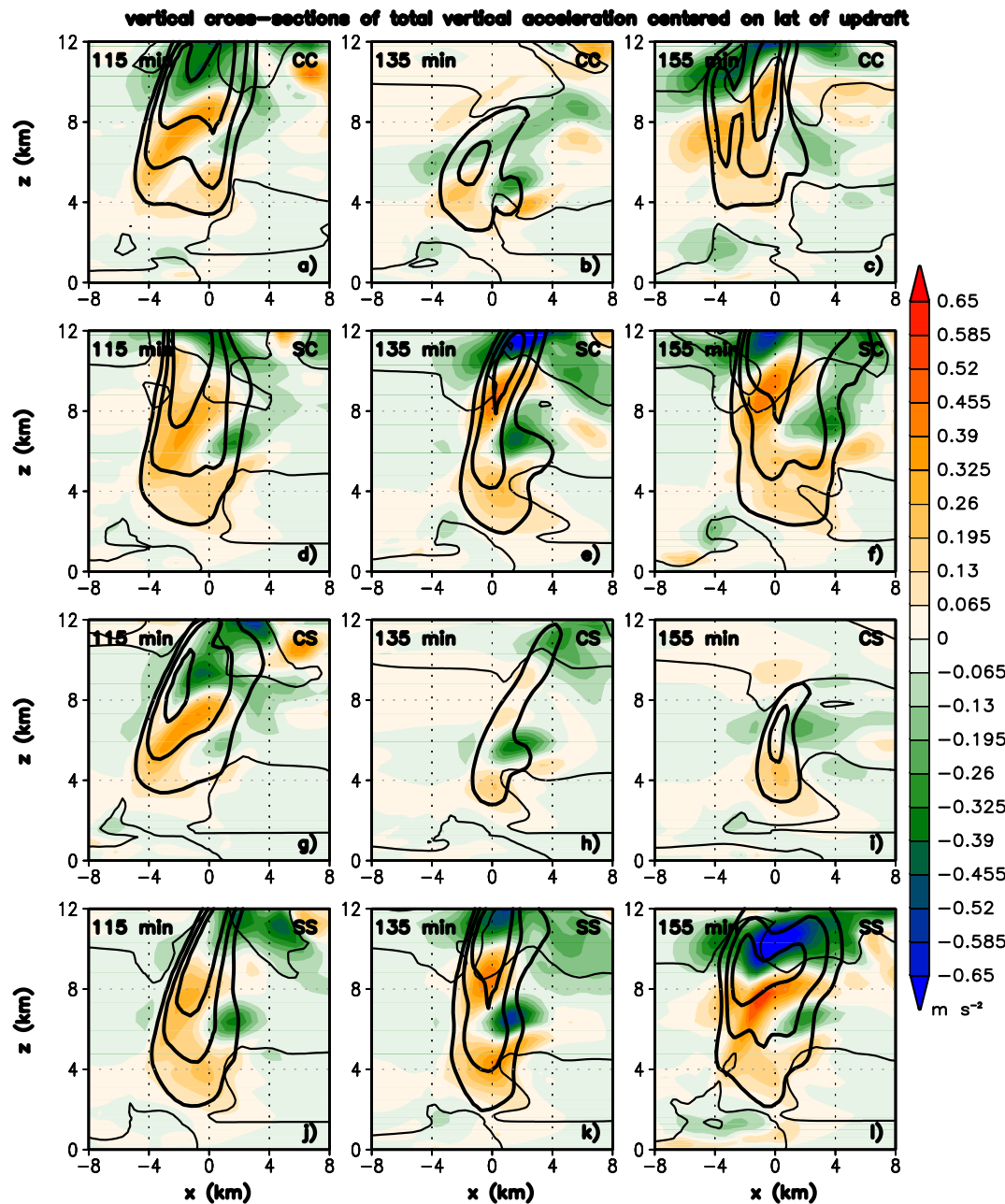


Figure 4.9: Vertical cross-sections of the updraft with total acceleration (shaded, as shown) and surface perturbation potential temperature (contoured in thin black, -1 K) and w (contoured in thick black, 15, 30, 45 m/s) for 115, 135, and 155 minutes.

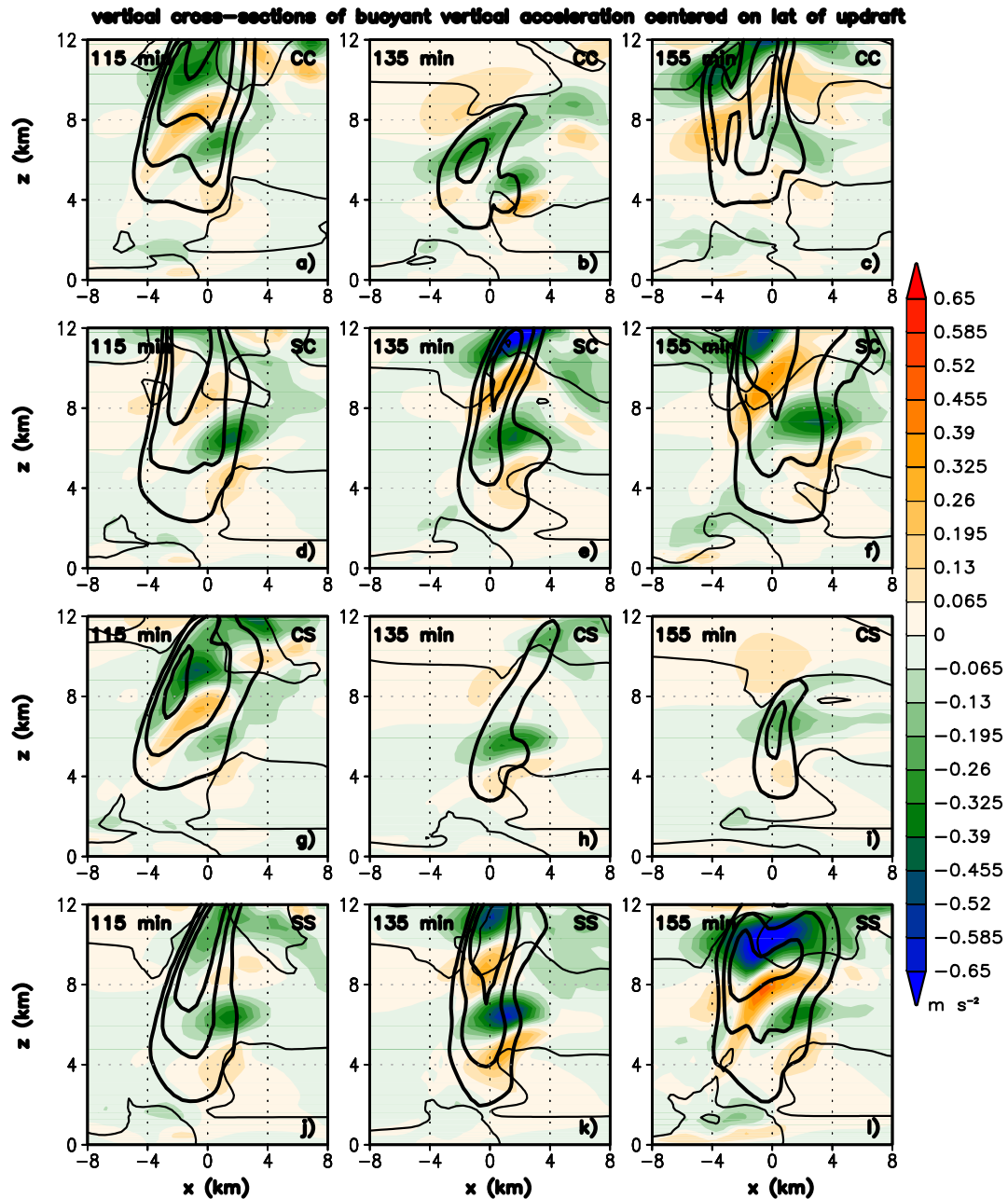


Figure 4.10: Vertical cross-sections of the updraft with buoyant acceleration (shaded, as shown) and surface perturbation potential temperature (contoured in thin black, -1 K) and w (contoured in thick black, 15, 30, 45 m/s) for 115, 135, and 155 minutes.

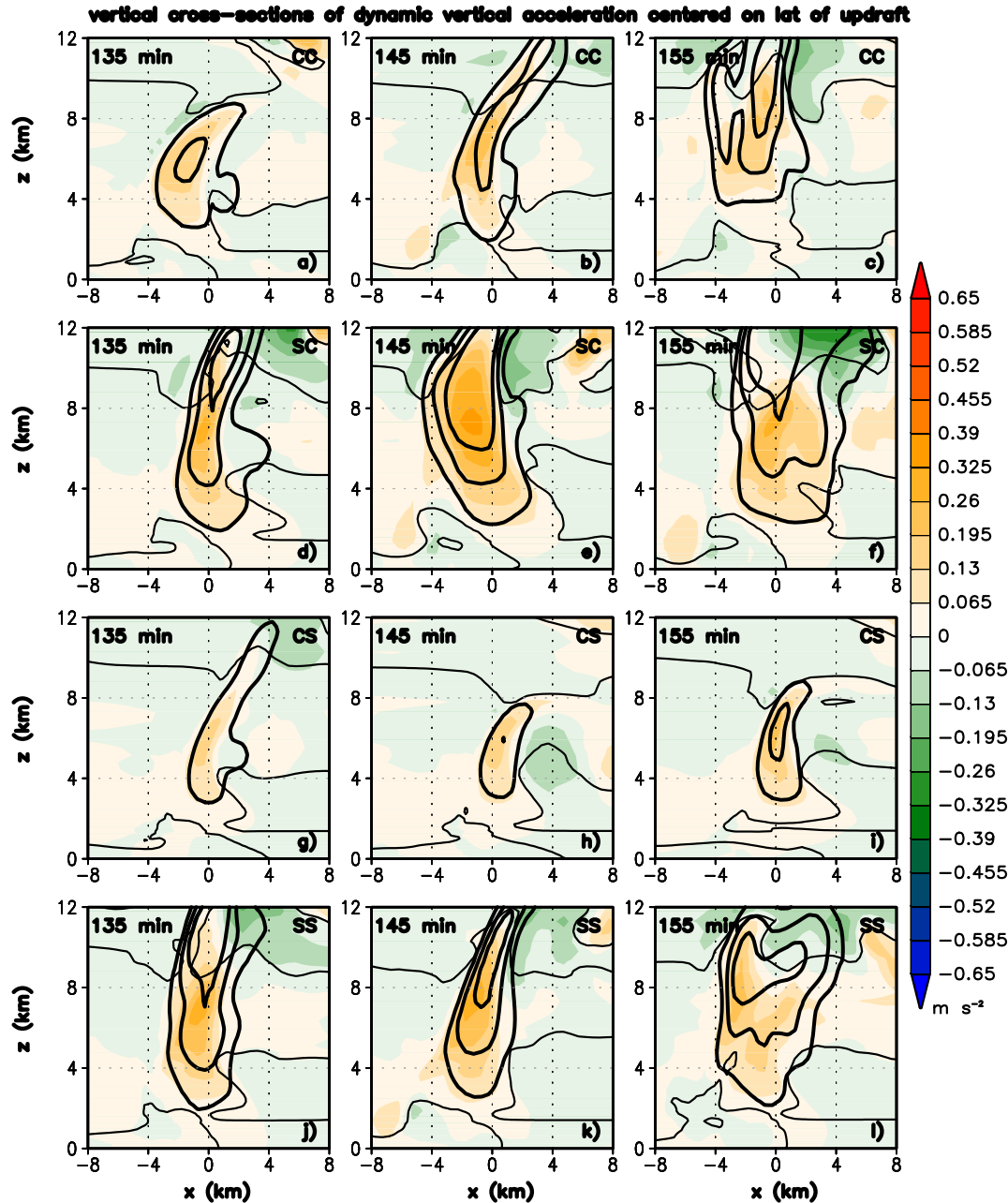


Figure 4.11: Vertical cross-sections of the updraft with dynamic acceleration (shaded, as shown) and surface perturbation potential temperature (contoured in thin black, -1 K) and w (contoured in thick black, 15, 30, 45 m/s) for 145, 135, and 165 minutes.

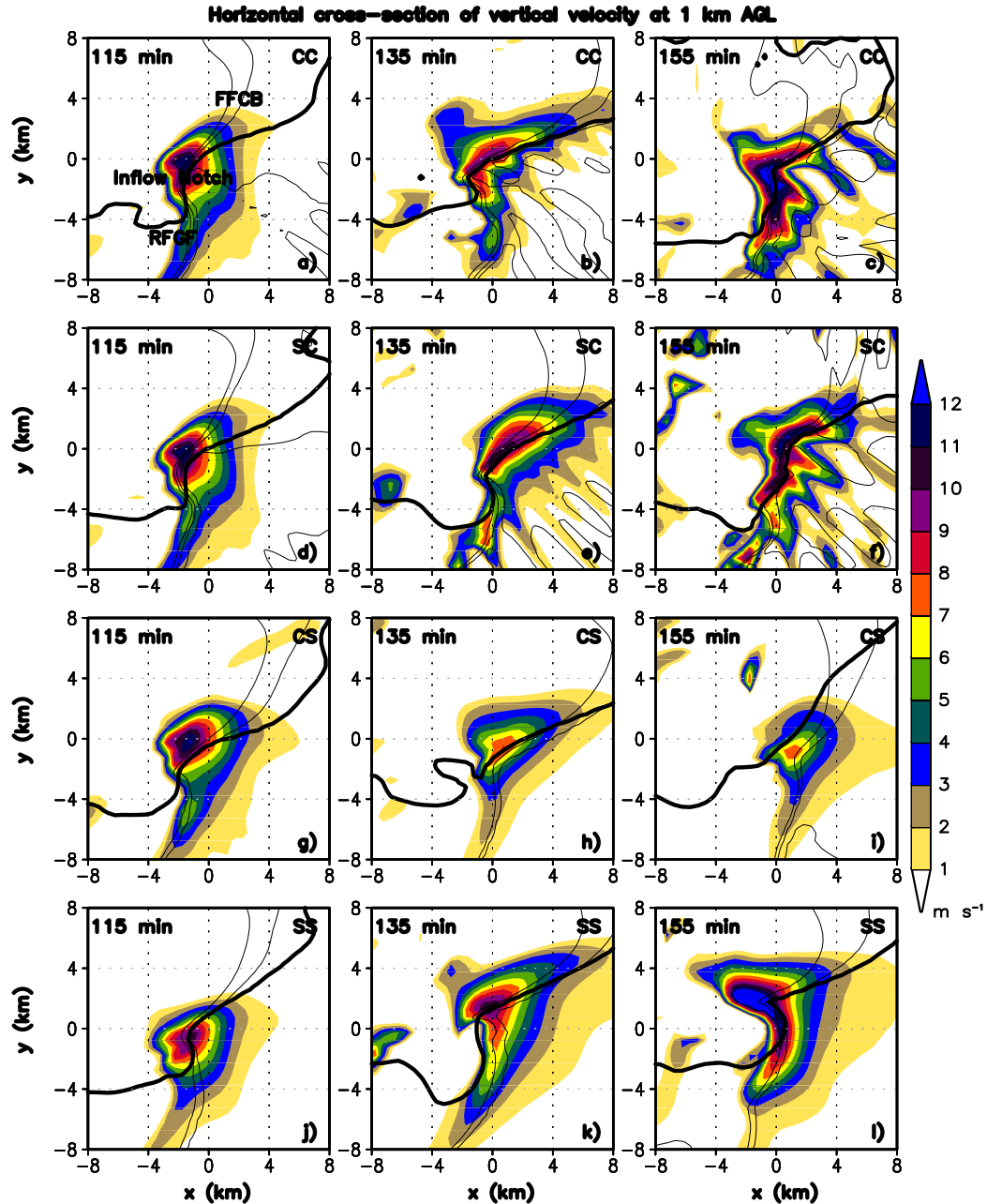


Figure 4.12: Horizontal cross-sections of the 1 km AGL updraft with w (shaded, as shown) and surface perturbation potential temperature (contoured in thin black, -2, -1 0 K) and 15 dBZ (contoured in thick black), at times 115, 135, and 155 minutes.

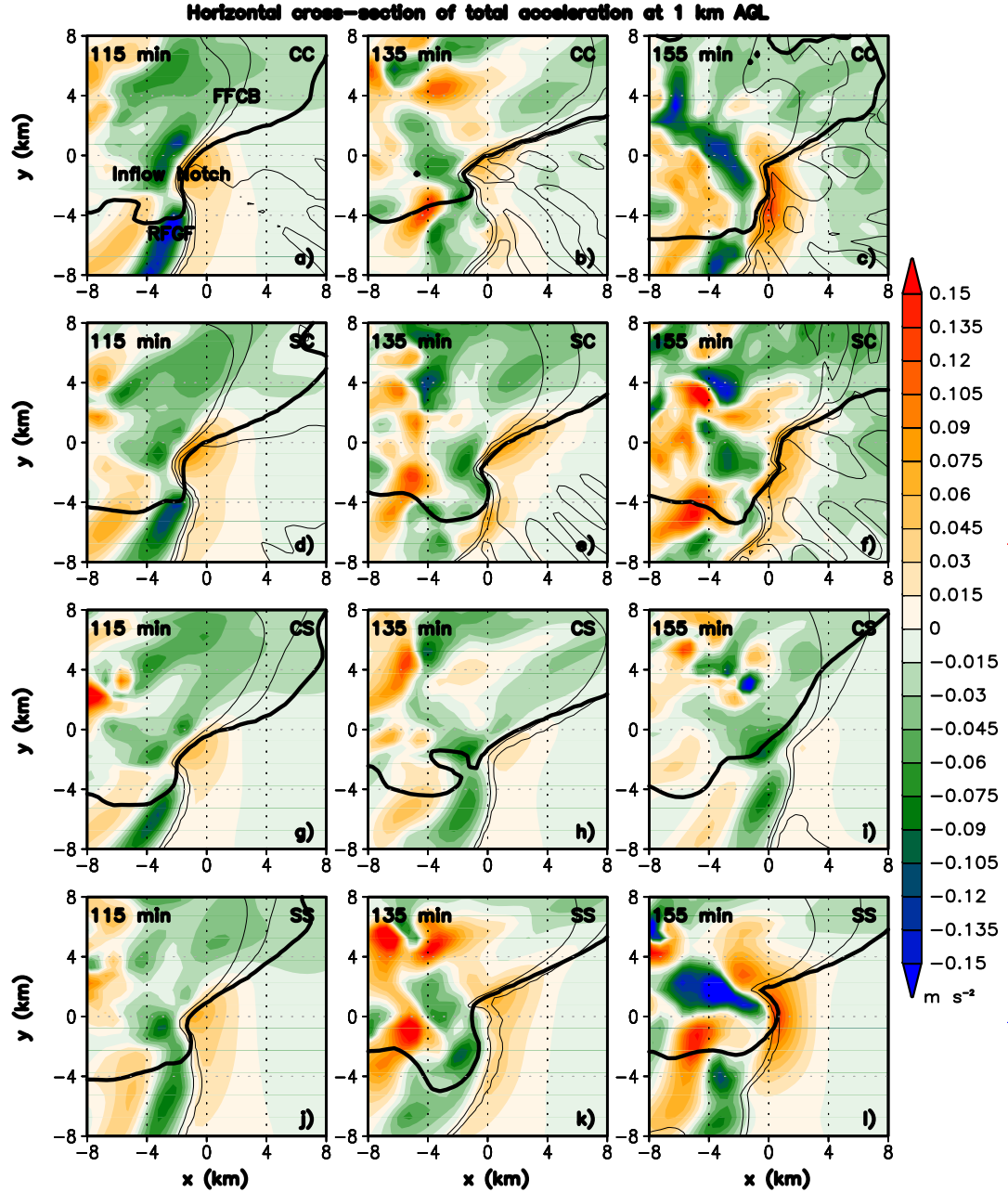


Figure 4.13: Horizontal cross-sections of the 1 km AGL total accelerations ($m s^{-2}$ shaded, as shown) and surface perturbation potential temperature (contoured in thin black, -2, -1 0 K) and 15 dBZ (contoured in thick black), at times 115, 135, and 155 minutes.

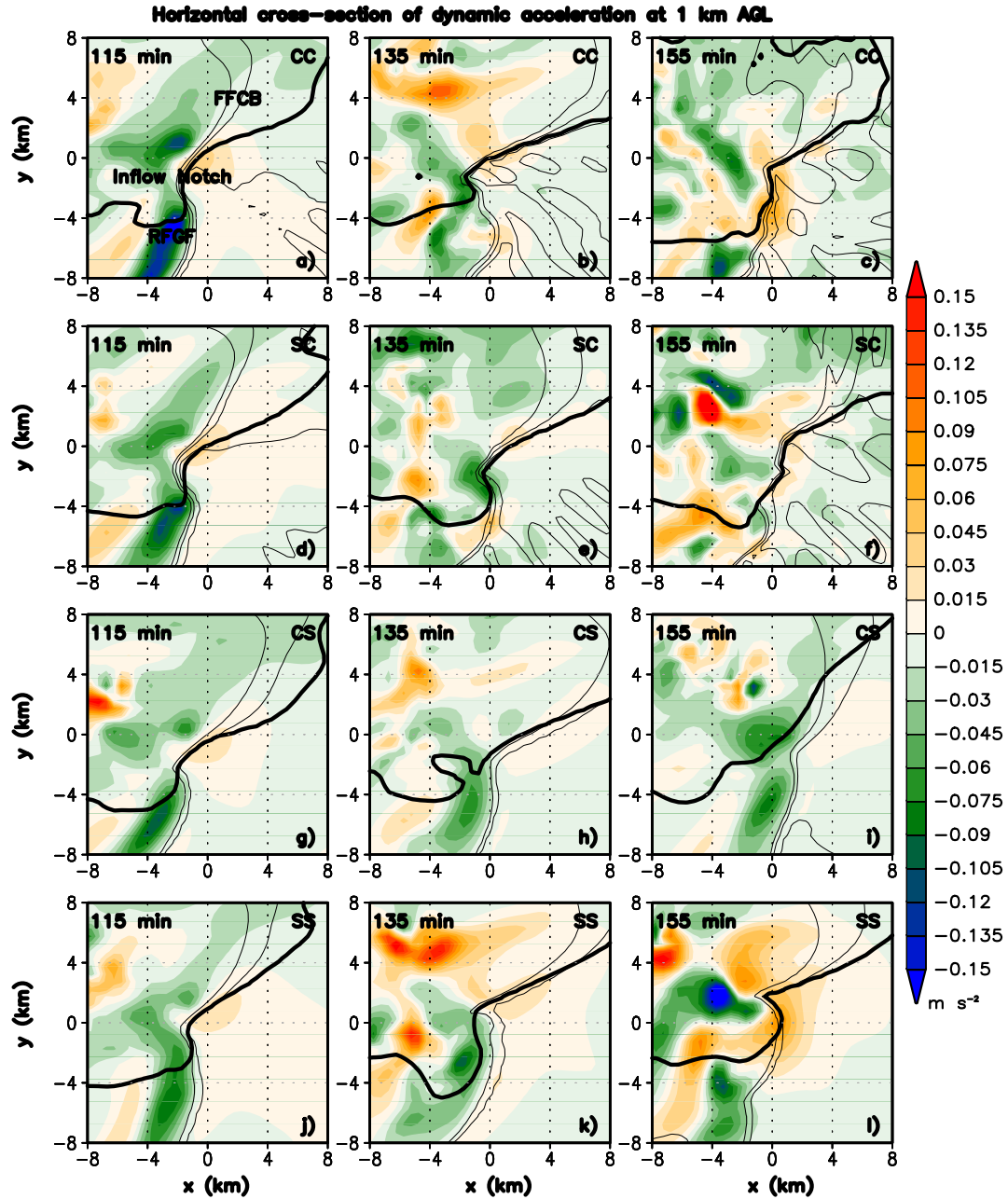


Figure 4.14: Horizontal cross-sections of the 1 km AGL dynamic accelerations (ms^{-2} shaded, as shown) and surface perturbation potential temperature (contoured in thin black, -2, -1 0 K) and 15 dBZ (contoured in thin black), at times 115, 135, and 155 minutes.

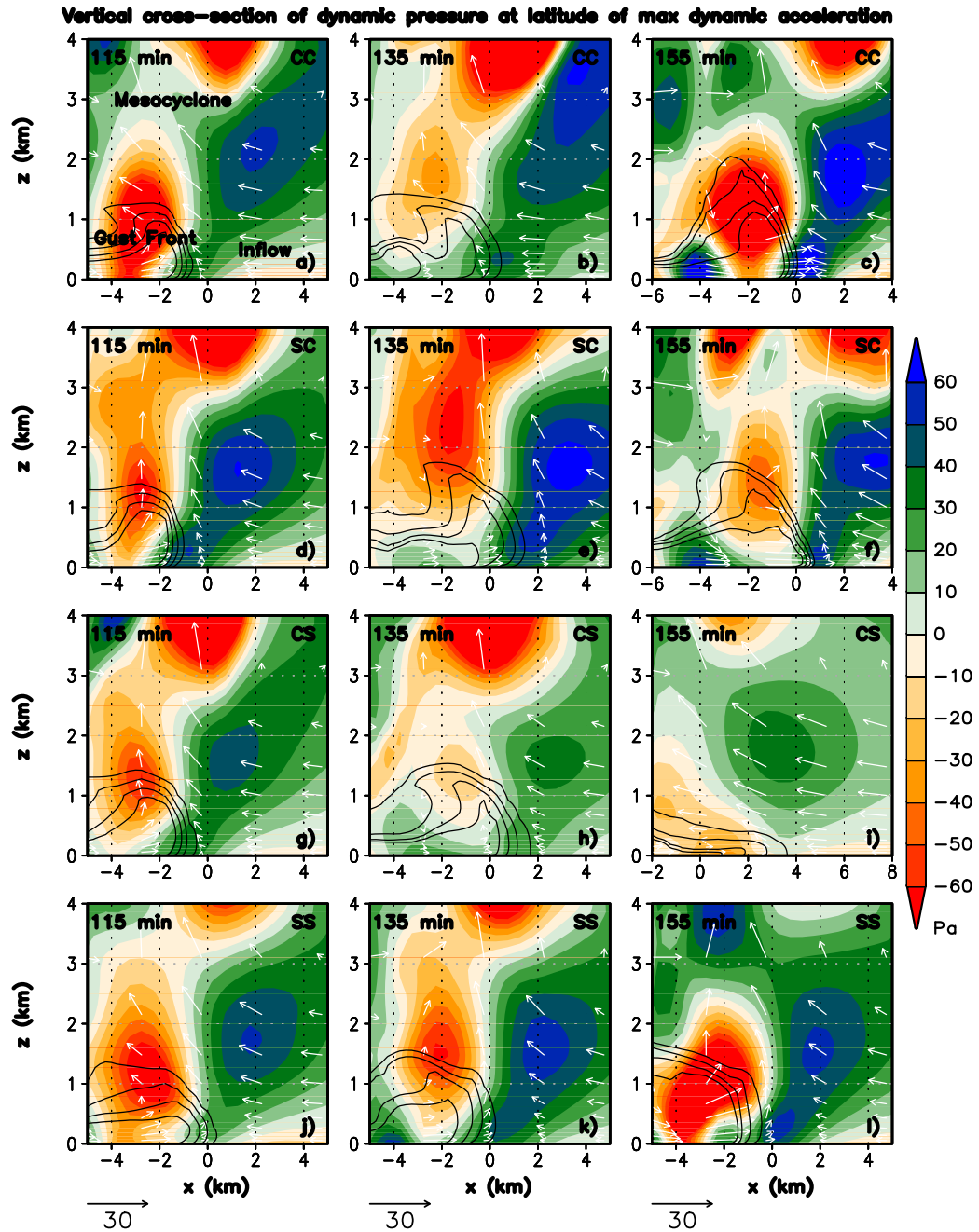


Figure 4.15: Vertical cross-sections of dynamic pressure perturbation (Pa), and perturbation potential temperature (contoured in thin black, -4, -3, -2, -1, and 0 K), and 15 dBZ (contoured in thick black), taken at the latitude of maximum buoyant acceleration. Wind vectors in the horizontal-vertical plane are shown as white arrows at times 115, 135, and 155 minutes.

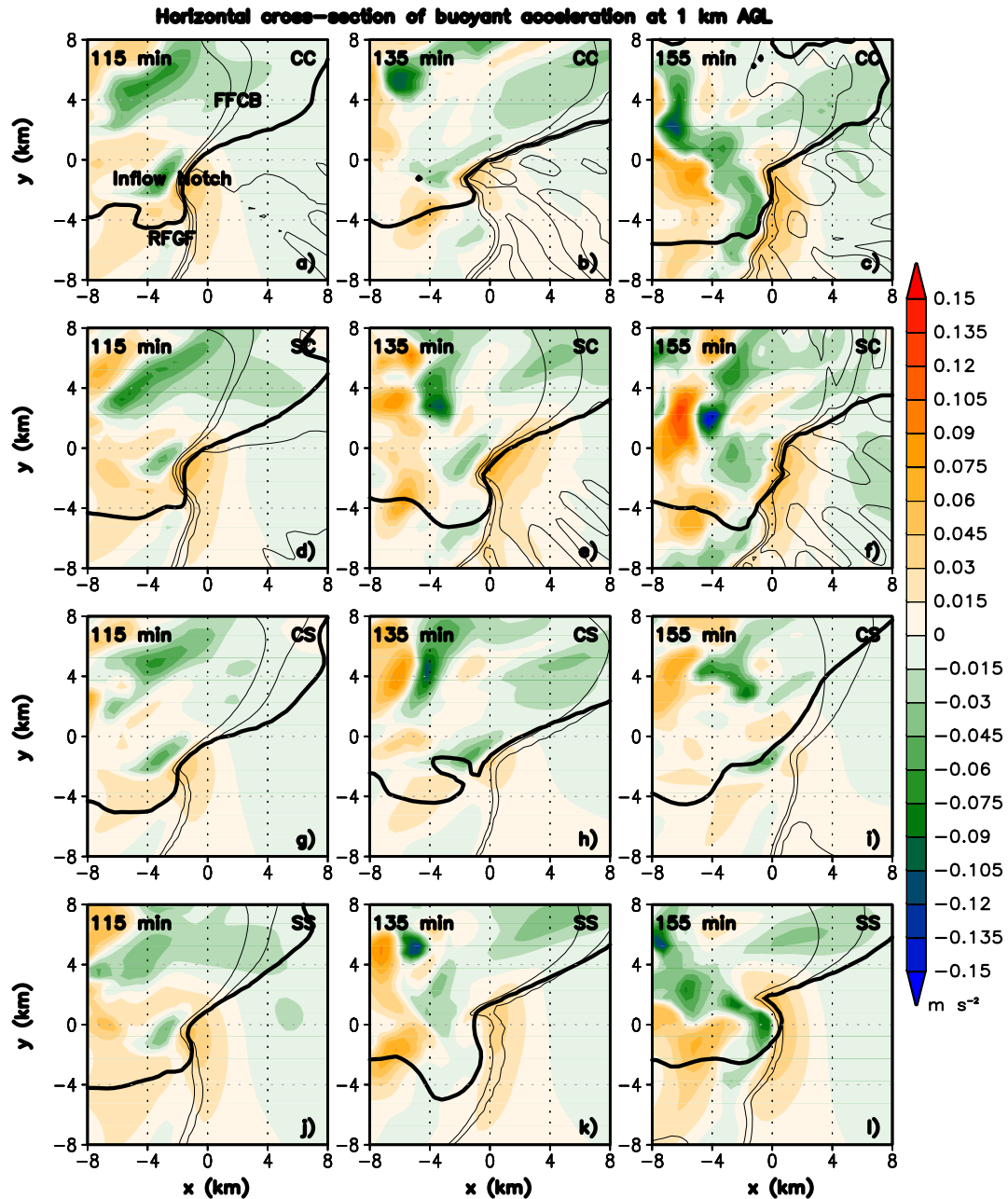


Figure 4.16: Horizontal cross-sections of the 1 km AGL buoyant accelerations (m s^{-2} shaded, as shown) and surface perturbation potential temperature (contoured thin black, -2, -10 K) and 15 dBZ (contoured in thick black), at times 115, 135, and 155 minutes.

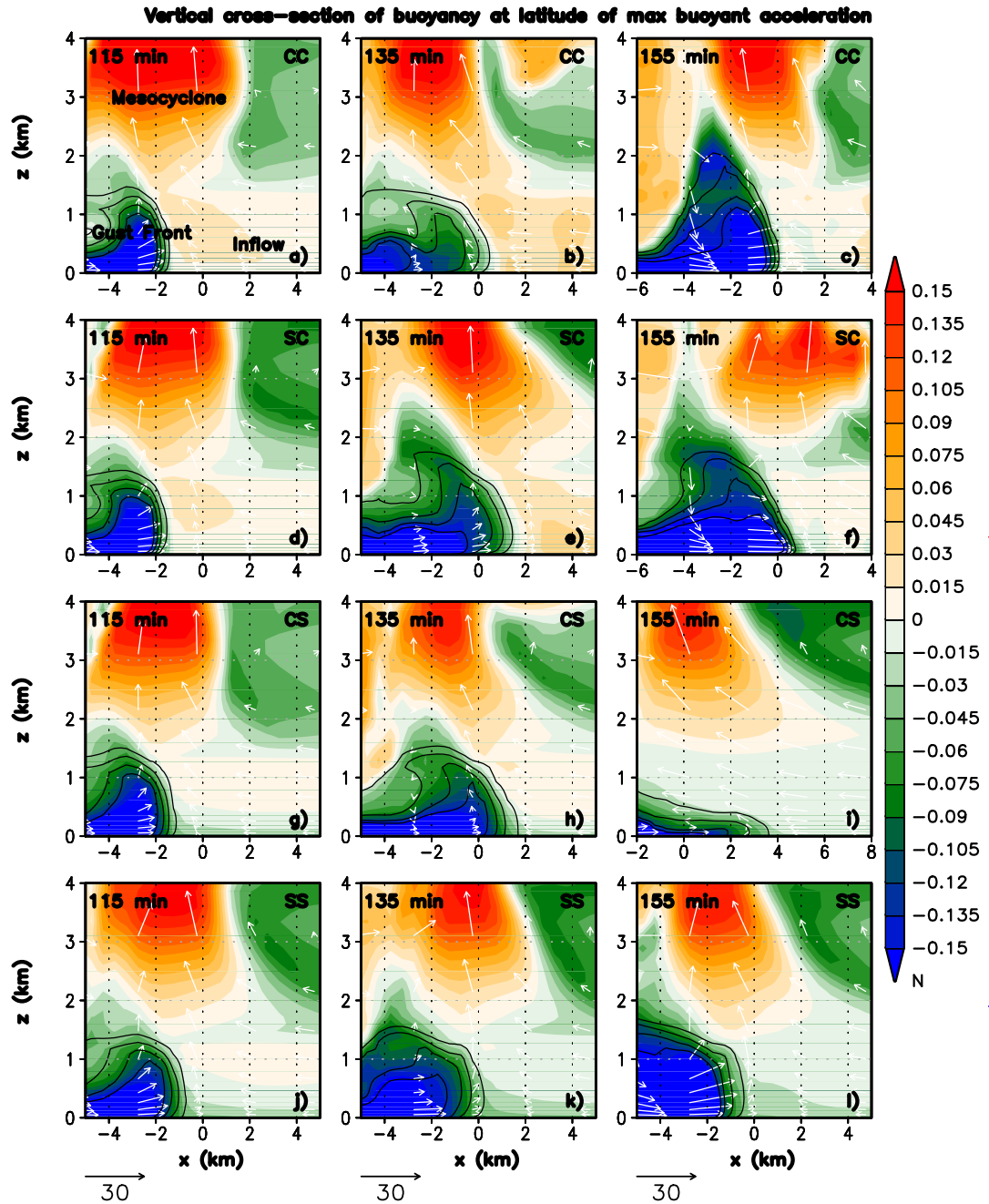


Figure 4.17: Vertical cross-sections of buoyancy (Pa), and perturbation potential temperature (contoured in thin black, -4, -3, -2, -1, and 0 K), and 15 dBZ (contoured in thick black), taken at the latitude of maximum buoyant acceleration at times 115, 135, and 155 minutes. Wind vectors in the horizontal-vertical plane are shown as white arrows at times 115, 135, and 155 minutes.

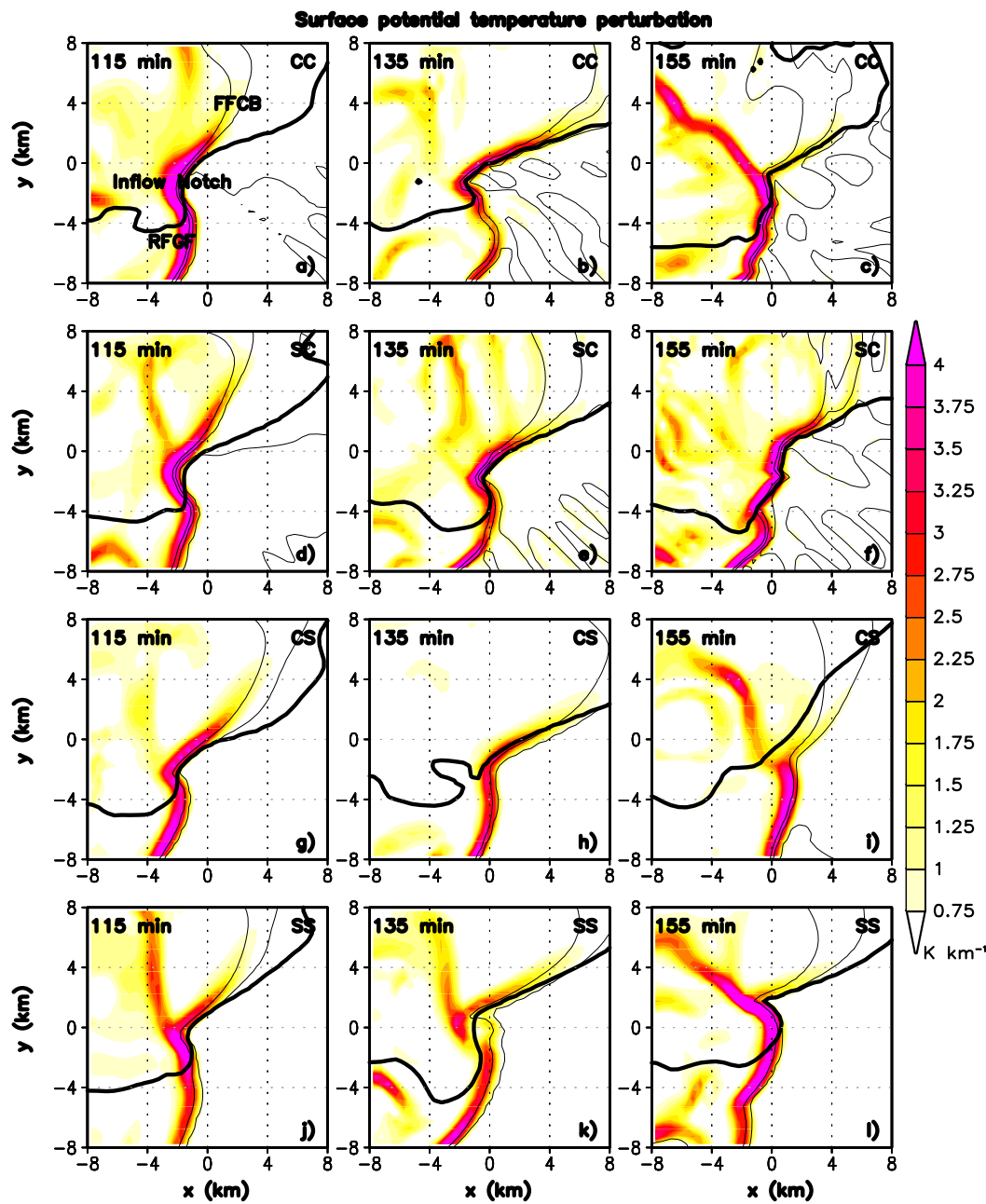


Figure 4.18: Horizontal cross-sections of the surface potential temperature perturbation (K contoured in thin black, -2 - 10 K) and 15 dBZ (contoured in thick black), at times 115, 135, and 155 minutes.

Chapter 5

Discussion

The most realistic simulation, COMBINED-SHADED, grew and intensified at first, but then at 115 minutes it decayed and never regained its former strength. This weakening occurs as the gravity wave moving through the midlevels passed the supercell and heated surrounding air. After the wave passed, the supercell decayed slowly before finally merging with the squall line at 5 hr. Our results contrast with previous work in interesting ways.

Most interesting, we identified a novel mechanism through which gravity waves may interact with mesocyclones. In contrast to the vorticity transfer model of Coleman and Knupp (2008), our results indicate that buoyancy perturbations may be most important in our circumstances. As the gravity wave moved through both COMBINED mesocyclones, upward accelerations in the updraft became blocked by negative buoyant accelerations aloft. This unbalanced the midlevel updraft and left both storms at half their initial strength. Eventually, this anomaly worked its way through the storm, so that 30 minutes later it had mostly disappeared. This shows a much different mechanism at work than the one described by Coleman and Knupp (2008). Either mechanism could result in a weakened mechanism. However, here, the transfer of heat, not vorticity, influenced how these mesocyclones developed.

In conjunction with the above paragraph, we determined that changes in environmental parameters were inconsequential to storm differences. The gravity wave and anvil shading acted not by changing key environmental parameters like CAPE and shear, but rather through the process described above. We highlight this finding to shed light in forecasting such systems, where environmental differences are thought to be key to storm differences. While important, other factors may determine a storm's outcome.

Anvil shading was not shown to alter the low-level wind profiles in such a way that enhanced vertical wind shear. This is in contrast to FM13, which saw changes to low-level shear

as the driving factor in supercell dissipation. Rather, our work showed that changes to the temperature gradient reduced low-level lifting. Additionally, buoyancy of the inflow was made more negative by anvil shading. Neither of these effects led to storm dissipation, as evidenced by the general health of SOLO-SHADED. However, once the storm weakened in COMBINED-SHADED, its changed low-level environment made regeneration impossible. Therefore, anvil shading led to storm dissipation through a different mechanism than those described by FM13.

The gravity wave evolved consistently with the findings of numerical experiments (Fovell 2002), as it modified the upstream environment's humidity, stability, and vertical wind profile. The prestorm environment underwent realistic changes, cooling near the surface as the anvil approached. Most importantly, the gravity wave in our experiment resembles observational finding from Bryan and Parker (2010). They observed a 1-mb decrease in surface pressure and increases in convective inhibition ahead of a squall line, indicating that a gravity wave had passed. While our environment was differently modified, these observations describe how a convectively triggered gravity wave can affect a real environments. The consistency between Bryan and Parker (2010) and our own research indicates that the interactions described in this paper may be more common than often thought.

Finally, preliminary sensitivity tests (not shown) indicate that varying the time of interaction could yield surprising outcomes. Moving the supercell by as little as 1 km, and thereby shifting the interaction time by minutes, could lead to no storm dissipation at all. These results indicate that the outcome depends on the state of the supercell: striking a mesocyclone at different stages of mesocyclogenesis leads to different outcomes. Though this is beyond the reach of this paper, future studies could benefit from further exploration of such sensitivity tests.

Chapter 6

Conclusion

6.1 Summary

Four simulations were run to investigate squall line-to-supercell interactions in the presence of anvil shading.

We have concluded that pre-merger interactions between squall lines and supercells could be detrimental to storm development. At the very least, it may lead to sporadic changes in supercell development. The gravity wave perturbed each supercell directly by raising temperatures aloft and generating negative buoyant accelerations in the COMBINED mesocyclones. Once the gravity wave had passed, the COMBINED-CLEAR storm recovered while the COMBINED-SHADED storm further weakened. Evidently, when anvil shading is present in the inflow of the supercell, it is even further weakened. The most realistic simulation, COMBINED-SHADED, led to the weakest supercell.

Contrary to our hypothesis, the changes in storm evolution were not the result of environmental effects, though indirect modifications to inflow buoyancy in COMBINED-SHADED played a part. Rather, the direct effects of the gravity wave on the storm itself were key. The combination of changes in low-level structure and diminished mesocyclone strength directly altered the supercell. Together, these led the COMBINED-SHADED supercell to nearly dissipate. Ultimately, both anvil shading and a gravity wave were needed to fully weaken the supercell. The process worked in two ways: 1) gravity wave weakened the midlevel mesocyclone through negative buoyant forcing and 2) anvil shading weakened low-level lifting by lowering buoyancy and surface temperature gradients.

6.2 Broader Implications

Our work shows that supercells spawning in the vicinity of nearby storms operate differently than their isolated counterparts. Because most of our knowledge comes from studying single supercells, we are limited when forecasting storms during outbreak events. While storm interactions in real time are complex, our results show a series of mechanisms governing these interactions. For example, when both anvil shading and a squall line were present, storm trajectory changed. Current algorithms, like the Storm Cell Identification and Tracking (SCIT) algorithm (Johnson et al. 1998), could be updated to act differently in similar situations. As our knowledge of these interactions grows, our predictive models and forecasting guidelines should evolve to account for storm-to-storm interactions. In moving toward short-fused forecasts based on high resolution models (see Stensrud et al. (2009) - Warn on Forecast program), we should ensure that the processes governing storm interactions are accurately represented in the model. Additionally, these types of forecasts will need to accurately capture all of the storms in a given environment in order to accurately forecast supercells. While many interactions remain unstudied, our work outlines a series of processes that should be included in future forecasting models.

6.3 Future Work

Many avenues of study remain unexplored. The differences between our results and the results of other studies underscores the complexity inherent in thunderstorm interactions. Interactions should be studied under different geometries, so that one may examine how the angle of incidence affects the interactions between gravity waves and supercells. Additionally, these interactions should be studied using different environments, as anvil shading appears to act differently in our environment than in that of FM13. Lastly, the time of interaction between gravity waves and supercells ought to be varied, as this may lead to different storm outcomes. For example, preliminary tests showed that changing the initial position of the supercell by as little as 0.5 km altered the timing of the storm interactions, affecting whether or not the supercell dissipated. Ultimately, a machine-learning oriented technique is likely needed to fully

explore this domain. The long-range goal should be to understand the general interaction between squall line-induced gravity waves and supercells, so that this framework could be applied to a variety of real-world circumstances.

Bibliography

- Adlerman, E. J. and K. K. Droege (2005). The dependence of numerically simulated cyclic mesocyclogenesis upon environmental vertical wind shear. *Monthly Weather Review* 133(12), 3595–3623.
- Adlerman, E. J., K. K. Droege, and R. Davies-Jones (1999). A numerical simulation of cyclic mesocyclogenesis. *Journal of the atmospheric sciences* 56(13), 2045–2069.
- Browning, K. A. (1964). Airflow and precipitation trajectories within severe local storms which travel to the right of the winds. *Journal of the Atmospheric Sciences* 21(6), 634–639.
- Bryan, G. H. and J. M. Fritsch (2002). A benchmark simulation for moist nonhydrostatic numerical models. *Monthly Weather Review* 130(12), 2917–2928.
- Bryan, G. H. and M. D. Parker (2010). Observations of a squall line and its near environment using high-frequency rawinsonde launches during vortex2. *Monthly Weather Review* 138(11), 4076–4097.
- Chou, M.-D., K.-T. Lee, S.-C. Tsay, and Q. Fu (1999). Parameterization for cloud longwave scattering for use in atmospheric models. *Journal of climate* 12(1), 159–169.
- Chou, M.-D., M. J. Suarez, C.-H. Ho, M. M. Yan, and K.-T. Lee (1998). Parameterizations for cloud overlapping and shortwave single-scattering properties for use in general circulation and cloud ensemble models. *Journal of climate* 11(2), 202–214.
- Coffer, B. E. and M. D. Parker (2015). Impacts of increasing low-level shear on supercells during the early evening transition. *Monthly Weather Review* 143(5), 1945–1969.
- Coleman, T. A. and K. R. Knupp (2008). The interactions of gravity waves with mesocyclones: Preliminary observations and theory. *Monthly Weather Review* 136(11), 4206–4219.
- Deardorff, J. W. (1980). Stratocumulus-capped mixed layers derived from a three-dimensional model. *Boundary-Layer Meteorology* 18(4), 495–527.
- Fovell, R. G. (2002). Upstream influence of numerically simulated squall-line storms. *Quarterly Journal of the Royal Meteorological Society* 128(581), 893–912.
- Frame, J. and P. Markowski (2010). Numerical simulations of radiative cooling beneath the anvils of supercell thunderstorms. *Monthly Weather Review* 138(8), 3024–3047.
- Frame, J. and P. Markowski (2013). Dynamical influences of anvil shading on simulated supercell thunderstorms. *Monthly Weather Review* 141(8), 2802–2820.
- French, A. J. and M. D. Parker (2008). The initiation and evolution of multiple modes of convection within a meso-alpha-scale region. *Weather and Forecasting* 23(6), 1221–1252.

- French, A. J. and M. D. Parker (2012). Observations of mergers between squall lines and isolated supercell thunderstorms. *Weather and Forecasting* 27(2), 255–278.
- French, A. J. and M. D. Parker (2014). Numerical simulations of bow echo formation following a squall line–supercell merger. *Monthly Weather Review* 142(12), 4791–4822.
- Fujita, T. (1958). Mesoanalysis of the illinois tornadoes of 9 april 1953. *Journal of Meteorology* 15(3), 288–296.
- Johnson, J., P. L. MacKeen, A. Witt, E. D. W. Mitchell, G. J. Stumpf, M. D. Eilts, and K. W. Thomas (1998). The storm cell identification and tracking algorithm: An enhanced wrs-88d algorithm. *Weather and forecasting* 13(2), 263–276.
- Kilduff, R. (1999). The interaction of a gravity wave with a thunderstorm. *Electronic poster, NOAA/National Weather Service*.
- Klemp, J. B. and R. B. Wilhelmson (1978). The simulation of three-dimensional convective storm dynamics. *Journal of the Atmospheric Sciences* 35(6), 1070–1096.
- Lemon, L. R. and C. A. Doswell III (1979). Severe thunderstorm evolution and mesocyclone structure as related to tornadogenesis. *Monthly Weather Review* 107(9), 1184–1197.
- Lin, Y.-L., R. D. Farley, and H. D. Orville (1983). Bulk parameterization of the snow field in a cloud model. *Journal of climate and applied meteorology* 22(6), 1065–1092.
- Maddox, R. A. (1976). An evaluation of tornado proximity wind and stability data. *Monthly Weather Review* 104(2), 133–142.
- Markowski, P., C. Hannon, J. Frame, E. Lancaster, A. Pietrycha, R. Edwards, and R. L. Thompson (2003). Characteristics of vertical wind profiles near supercells obtained from the rapid update cycle. *Weather and forecasting* 18(6), 1262–1272.
- Markowski, P. and Y. Richardson (2010). *Mesoscale Meteorology in Midlatitudes*. Wiley-Blackwell.
- Markowski, P. M., E. N. Rasmussen, J. M. Straka, and D. C. Dowell (1998). Observations of low-level baroclinity generated by anvil shadows. *Monthly weather review* 126(11), 2942–2958.
- Miller, D. A. and F. Sanders (1980). Mesoscale conditions for the severe convection of 3 april 1974 in the east-central united states. *Journal of the Atmospheric Sciences* 37(5), 1041–1055.
- Nicholls, M. E., R. A. Pielke, and W. R. Cotton (1991). Thermally forced gravity waves in an atmosphere at rest. *Journal of the atmospheric sciences* 48(16), 1869–1884.
- Parker, M. D. and R. H. Johnson (2004). Structures and dynamics of quasi-2d mesoscale convective systems. *Journal of the atmospheric sciences* 61(5), 545–567.
- Richardson, Y. P., K. K. Droegemeier, and R. P. Davies-Jones (2007). The influence of horizontal environmental variability on numerically simulated convective storms. part i: Variations in vertical shear. *Monthly Weather Review* 135(10), 3429–3455.
- Schoenberg Ferrier, B. (1994). A double-moment multiple-phase four-class bulk ice scheme. part i: Description. *Journal of the Atmospheric Sciences* 51(2), 249–280.

- Stensrud, D. J., M. Xue, L. J. Wicker, K. E. Kelleher, M. P. Foster, J. T. Schaefer, R. S. Schneider, S. G. Benjamin, S. S. Weygandt, J. T. Ferree, et al. (2009). Convective-scale warn-on-forecast system: A vision for 2020. *Bulletin of the American Meteorological Society* 90(10), 1487–1500.
- Thompson, R. L., R. Edwards, J. A. Hart, K. L. Elmore, and P. Markowski (2003). Close proximity soundings within supercell environments obtained from the rapid update cycle. *Weather and Forecasting* 18(6), 1243–1261.
- Weisman, M. L. and J. B. Klemp (1982). The dependence of numerically simulated convective storms on vertical wind shear and buoyancy. *Monthly Weather Review* 110(6), 504–520.
- Weisman, M. L. and J. B. Klemp (1984). The structure and classification of numerically simulated convective storms in directionally varying wind shears. *Monthly Weather Review* 112(12), 2479–2498.
- Wilhelmsen, R. B. and L. J. Wicker (2001). Numerical modeling of severe local storms. In *Severe convective storms*, pp. 123–166. Springer.
- Wolf, R., R. Przybylinski, and P. Berg (1996). Observations of a merging bowing segment and supercell. In *Preprints, 18th Conf. on Severe Local Storms, San Francisco, CA, Amer. Meteor. Soc*, pp. 740–745.
- Ziegler, C. L., E. R. Mansell, J. M. Straka, D. R. MacGorman, and D. W. Burgess (2010). The impact of spatial variations of low-level stability on the life cycle of a simulated supercell storm. *Monthly Weather Review* 138(5), 1738–1766.

Vita

Michael Montalbano was born to Joe and Sharon Montalbano in Hammonton, New Jersey on March 26, 1993. After graduating from Hammonton High School on June 3, 2011, he attended the College of New Jersey, where he received a Bachelor of Science in Physics in May 2015. He taught Physics 211, 213, and labs at the South Dakota School of Mines and Technology between 2016 and 2019.